



Article

Self-Starting Improvement and Performance Enhancement in Darrieus VAWTs Using Auxiliary Blades and Deflectors

Farzad Ghafoorian ^{1,*} , Erfan Enayati ², Seyed Reza Mirmotahari ²  and Hui Wan ¹

¹ Department of Mechanical and Aerospace Engineering, University of Colorado, Colorado Springs, CO 80918, USA; hwan@uccs.edu

² Department of Energy Conversion, School of Mechanical Engineering, Iran University of Science and Technology, Tehran 16846-13114, Iran; e_enayati@mecheng.iust.ac.ir (E.E.); reza_mirmotahari@mecheng.iust.ac.ir (S.R.M.)

* Correspondence: fghafoor@uccs.edu

Abstract: The Darrieus vertical axis wind turbine (VAWT) is categorized as a lift-based turbomachine. It faces challenges in the low tip speed ratio (TSR) range and requires initial torque for the starting operation. Ongoing efforts are being made to enhance the turbine's self-starting capability. In this study, Computational Fluid Dynamics (CFD) simulations were utilized to tackle the identified challenge. The Unsteady Reynolds-Averaged Navier–Stokes (URANS) approach was employed, combined with the shear–stress transport (SST) $k - \omega$ turbulence model, to resolve fluid flow equations. The investigation focused on optimizing the placement of auxiliary blades by considering design parameters such as the pitch angle and horizontal and vertical distances. The goal was to increase the turbine efficiency and initial torque in the low-TSR range while minimizing efficiency loss at high-TSR ranges, which is the primary challenge of auxiliary blade installation. Implementing the auxiliary blade successfully extended the rotor's operational range, shifting the rotor operation's onset from TSR 1.4 to 0.7. The optimal configuration for installing the auxiliary blade involves a pitch angle of 0° , a horizontal ratio of 0.52, and a vertical ratio of 0.41. To address the ineffectiveness of auxiliary blades at high-TSRs, installing deflectors in various configurations was explored. Introducing a double deflector can significantly enhance the overall efficiency of the conventional Darrieus VAWT and the optimum rotor with the auxiliary blade by 47% and 73% at TSR = 2.5, respectively.

Keywords: Darrieus VAWT; auxiliary blades; deflectors; self-starting capability; low and high-TSR range; blade stall



Citation: Ghafoorian, F.; Enayati, E.; Mirmotahari, S.R.; Wan, H.

Self-Starting Improvement and Performance Enhancement in Darrieus VAWTs Using Auxiliary Blades and Deflectors. *Machines* **2024**, *12*, 806. <https://doi.org/10.3390/machines12110806>

Academic Editors: Francesco Papi and Mircea Neagoe

Received: 16 October 2024

Revised: 6 November 2024

Accepted: 11 November 2024

Published: 14 November 2024



Copyright: © 2024 by the authors. Licensee MDPI, Basel, Switzerland. This article is an open access article distributed under the terms and conditions of the Creative Commons Attribution (CC BY) license (<https://creativecommons.org/licenses/by/4.0/>).

1. Introduction

The rapid growth of the global population and the environmental impacts of fossil fuel use are driving an urgent search for renewable energy sources [1]. According to the International Energy Agency (IEA), the renewable energy capacity must triple by 2030 to achieve 61% of electricity generation from renewable sources, with most of this growth coming from wind and solar PV [2]. In particular, wind energy has garnered significant attention due to its abundant, pollution-free, clean, and cost-effective characteristics, making it a focal point of numerous studies [3]. Forecasts indicate that the capacity for extractable wind energy is anticipated to rise to approximately 30,000 GW by 2030, compared to less than 1000 GW in 2021 [4].

Wind turbines are classified into two main types based on the orientation of their axis: horizontal axis wind turbines (HAWTs) and vertical axis wind turbines (VAWTs) [5]. Despite generally being less efficient than HAWTs, VAWTs have garnered considerable interest due to their unique advantages. Their ability to capture wind from all directions makes them ideal for urban environments and effective in regions with low wind speeds [6,7]. Furthermore, the vertical design allows essential mechanical components to be installed closer to the ground, which reduces noise, size, and maintenance costs [8]. VAWTs are

classified into two main types: Savonius turbines and Darrieus turbines. Savonius turbines operate primarily on the principle of drag, whereas Darrieus turbines harness lift forces [9]. Savonius turbines typically have low efficiency in energy conversion and are best suited for small-scale applications [10]. In contrast, Darrieus turbines can achieve high power coefficients (C_p). However, due to their aerofoils being largely stalled at low speeds, they produce a minimal starting torque and struggle with self-starting [11]. Numerous techniques have been utilized to enhance the aerodynamic performance of Darrieus VAWTs, aiming to boost their efficiency and self-starting capability. These methods encompass intervention measures in the rotor geometry's conceptual design and flow improvement techniques [12]. The self-starting capability poses a significant challenge for $TSR < 1$. This issue is further exacerbated when the blade is positioned within an azimuth angle range of 100° to 253° . To address this problem, an increase in the blade numbers was introduced; however, a C_p reduction in the high- TSR range was observed [13]. Mohamed et al.'s [14] research provides comprehensive insights into the self-starting capabilities across different $TSRs$. Their findings confirm the occurrence of these challenges at azimuth angles where a blade resides within the wake area of another blade. This phenomenon underscores the necessity for increased drag force within the lower TSR range.

Extensive research has been conducted to enhance rotor performance by effectively manipulating flow using external objects such as guide vanes, control rods, deflectors, and curtains. These studies aim to optimize flow direction, control restraining forces, and reduce drag to improve overall rotor efficiency [15]. Enhancing the velocity of the incoming flow, commonly referred to as flow augmentation directed toward Darrieus VAWT, is of utmost importance. Notably, an increase in the Reynolds number from 10^4 to 10^6 significantly enhances the C_p , elevating it from 0.15 to 0.5 [16]. Utilizing an external object as a drag-inducing mechanism positioned in front of the Darrieus rotor has enhanced torque and improved the rotor's self-starting capability by up to 41.7%, achieved by reducing unfavorable drag [17]. Two types of semi-directional guide vanes with unique geometries, one airfoil-shaped and the other curved-shaped as an external body, increased the rotor's operating range from 0.5 to 0.8 and significantly increased its efficiency [18,19]. The existence of a deflector can significantly affect the flow direction and drag reduction. In a recent study, it was found that the utilization of a porous deflector improved the rotor's performance and self-starting capability. Notably, a deflector with a porosity of 0.6 demonstrated superior performance compared to a traditional deflector [20]. The study conducted by Layeghmand et al. [21] demonstrates that an airfoil-shaped deflector exhibits superior aerodynamic performance compared to a plate deflector. This improved performance is attributed to the airfoil-shaped deflector's ability to delay flow separation when installed at an optimal angle. In general, research has indicated that incorporating an external object to direct airflow towards the rotor, specifically through wedge-shaped deflectors and vented blade flaps, has significantly enhanced the performance of VAWTs compared to other external objects [22].

As mentioned before, another way to improve the performance of a VAWT is to modify the conceptual design of its rotor blades, in addition to enhancing the airflow direction by an external body. Modifications made to the airfoil blade can significantly influence the aerodynamic forces experienced by the blade. Even seemingly minor alterations, such as variations in thickness or surface roughness like a thick aerodynamic profile, can markedly affect the aerodynamic characteristics and enhance the lift force generated by the airfoil [23]. One of the geometric adjustments involves enhancing the pitch angle of the blades and employing asymmetric airfoil profiles [24]. A numerical analysis indicated that substituting a conventional airfoil with a J-shaped airfoil resulted in a significant efficiency enhancement of 25% to 70% in the performance of Darrieus rotor turbines within the low- TSR range. However, due to the swirling flow trapped on the suction side of the airfoil, the efficiency declined at higher rotational velocities [25]. Incorporating a J-shaped blade in the Darrieus VAWT has resulted in a notable 59% enhancement in turbine efficiency, as reported in another numerical study utilizing a more precise LES numerical method [26].

An additional geometric modification that can be made to Darrieus rotor blades involves creating a cavity on either the pressure or the suction side. These alterations have enhanced the rotor's aerodynamic performance, yielding improvements of up to 7% in lift force [27]. It is imperative to highlight that the enhancement of Darrieus VAWT extends beyond mere improvements in C_p . A range of methodologies have been employed to optimize flow dynamics and enhance the aerodynamic efficiency of the rotor by mitigating the impacts of dynamic and rotational stall phenomena while implementing effective flow control strategies. Importantly, these methods may lead to a reduction in C_p across various TSR ranges [28]. Techniques such as the integration of vortex cavities and slotted blades illustrate this intricate process of optimization [29]. Ibrahim et al. [30] demonstrated that the implementation of the vortex cavity on the airfoil suction side significantly enhanced efficiency from 0.375 to 0.435 in the high-TSR range. Furthermore, this configuration proved effective in improving both the torque and self-starting capability within the azimuth angle range of 0° to 150° . One such method involves utilizing the Kline and Fogleman approach to design the rotor blades, which introduces steps on the blade, thereby sacrificing some efficiency for the better control of rotational and dynamic stall phenomena [31]. Another practical method for enhancing the aerodynamic performance of Darrieus VAWTs involves utilizing Doubled-Row configurations. This approach entails situating an identical blade adjacent to the primary blade, potentially elevating power and torque coefficients by up to 300% [32]. In a study by Khalid et al. [33], it was demonstrated that aligning the second row of blades with the main blades represented the least effective configuration for enhancing self-starting. Conversely, the most optimal configuration is achieved when the design incorporates a 90° phase difference in the row of blades. A similar study highlighted that adding a blade row to the rotor does not uniformly enhance the turbine's power coefficient across all TSRs. Moreover, this alteration can lead to reduced efficiency at TSRs exceeding 3. Notwithstanding, the inclusion of an extra row of blades has the potential to enhance the rotor's self-starting capability by increasing C_m and C_p in the initial TSRs [34]. It is essential to consider that the diameter, height, and chord length of the inner row of blades may not precisely match those of the outer row. Research indicates that raising the height of the inner row of blades while reducing their diameter leads to an overall improvement in the turbine's C_p [35]. To enhance the rotor's self-starting capability, auxiliary blades were introduced alongside the main blades as an alternative to adding an extra row of blades. This configuration was aimed at improving the rotor's aerodynamic performance. The findings revealed that the rotor's efficiency showed an enhancement at lower TSRs but decreased at higher TSRs in comparison to the conventional rotor design [10,36]. The inclusion of the auxiliary blade demonstrated not only an ability to increase the torque coefficient by up to 84% and enhance the self-starting capability but also to widen the rotor's operating range from TSR 0.4 to 1.9 [37].

Based on the findings from the literature review, it has been identified that the self-starting capability presents a significant challenge for lift-based VAWTs, particularly Darrieus VAWTs. A proposed solution to enhance the initial torque for lift-based rotors and improve the self-starting capability involves the integration of an auxiliary blade alongside the primary blade to fulfill the initial torque requirements. However, prior research has predominantly concentrated on the incorporation of auxiliary blades and the performance of rotors within the low-TSR range. This focus has resulted in a lack of consideration for the overall performance and efficiency metrics, including the C_p values. Furthermore, comprehensive investigations into the potential adverse effects of adding auxiliary blades on the rotor aerodynamic performance and the assessment of rotor torque and overall efficiency, particularly within a high-TSR range, have been insufficient. These factors necessitate further investigation by assessing performance maps and examining strategies to mitigate the adverse effects of adding an auxiliary blade on rotor performance within the high-TSR range. In this study, we have investigated the effects of installing an auxiliary blade and developing a blade set to enhance the self-starting capability and efficiency of the rotor within a low-TSR range. Additionally, to address the previous research gap, our

approach begins with an analysis of the design parameters associated with the auxiliary blade, focusing on its optimal installation position concerning the primary blade, which includes considerations of both vertical and horizontal distances as well as the pitch angle. In the subsequent stage, we aim to improve performance further by incorporating an external object and optimizing the airflow direction towards the rotor, representing a substantial advancement compared to previous findings. To demonstrate the superiority and originality of the current study, as well as to address existing research gaps, the overall structure of the manuscript is organized as follows:

- This study examines the integration of an auxiliary blade into a conventional Darrieus rotor. Additionally, it investigates the essential conceptual design parameters necessary for effectively incorporating the auxiliary blade, including pitch angle, vertical distance, and horizontal distance. Previous research has primarily focused on the auxiliary blade at a single position, without considering its comprehensive design parameters.
- In addition to optimizing the positioning of the auxiliary blade relative to the main blade to enhance self-starting capabilities and efficiency within the low-TSR range, there is a concurrent focus on improving overall efficiency in the high-TSR range and addressing the primary challenge associated with the auxiliary blade, which has not been thoroughly examined in prior studies. To achieve this aim, an external object is strategically placed in front of the rotor for evaluation purposes.
- In this study, the deflector has been identified as an external object that effectively directs airflow toward the rotor. To ensure the optimum efficiency of deflector installation on the aerodynamic performance of the rotor at the high-TSR range, three distinct configurations, namely double deflectors and top and bottom deflectors, have been arranged in front of the rotor.
- In addition to assessing the turbine's performance map, a comprehensive analysis of flow physics has been conducted regarding both the auxiliary blade and deflector installations. This investigation emphasizes the examination of velocity, pressure, and vorticity fields. By scrutinizing these results, the study not only evaluates the impact of the auxiliary blade and deflector on turbine efficiency but also assesses their influence on the potential occurrence of dynamic stall on the blade. This methodology signifies a notable advancement in comparison to previous research endeavors.

2. Case Study Discretion

The current investigation pertains to the selection of a Darrieus VAWT utilizing the geometric configuration developed by Castelli et al. [38]. The pertinent design parameters are detailed in Table 1. In addition, Figure 1a presents a diagram depicting the rotor with the auxiliary blade and double deflector positioned in front of it. Also, to clarify the design aspects of the auxiliary blade, a detailed view of the blade set with an auxiliary blade is presented in Figure 1b. Additionally, Figure 1d provides an overview of the computational domain and the corresponding dimensions of the rotor from lateral sides, as well as the inlet and outlet. Furthermore, Figure 1e illustrates the procedural steps involved in design, meshing, CFD simulation, and data post-processing. Initially, the CAD model was developed using DesignModeler, which is part of the Ansys Workbench package. Subsequently, the model was discretized through the meshing process in the Ansys Meshing package. Following this, boundary conditions and appropriate simulation solver settings were established using Fluent. Finally, the flow field contours were analyzed and visualized through Tecplot.

Table 1. Geometric characteristics of the simulated Darrieus VAWT [39].

Quantity	Value
Number of blades	3
Blade chord length	85.8 (mm)
Rotor diameter	1030 (mm)
Rotor solidity	0.5
Blade airfoil profile	NACA0021

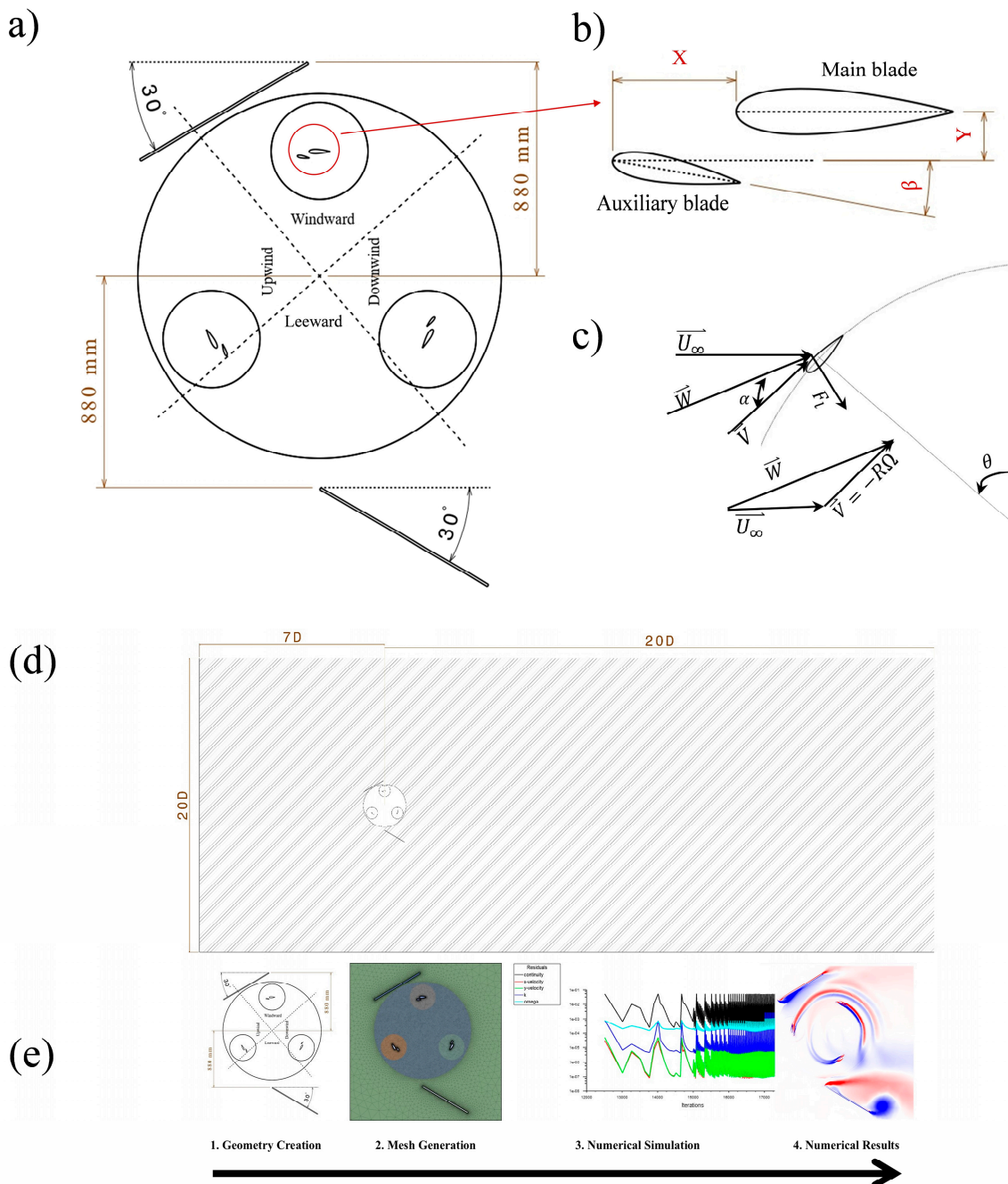


Figure 1. Darrieus wind turbine schematic: (a) Darrieus VAWT with auxiliary blades and double deflectors, (b) blade set, (c) lift force and velocities on a blade, (d) computational domain dimension, and (e) compendium process for current study.

As presented in Figure 1, implementing an auxiliary blade on the control case rotor is the initial step taken to enhance the self-starting capability. Subsequently, to address

potential inefficiencies in the modified rotor, the deflector with the modified rotor with the auxiliary blade is incorporated, featuring distinct deflector configurations. The deflectors, measuring 0.8 m in length and 0.01 m in width, are integrated to mitigate operational challenges. Moreover, Figure 1b presents a detailed illustration of the blade set, which encompasses both the main and auxiliary blades positioned at their exact locations. This illustration highlights three critical design parameters of the auxiliary blade: the pitch angle, denoted as “ β ”, which is defined as the installation angle of the auxiliary blade concerning its chord; the vertical distance, denoted as “ Y ”, which is measured from the chord lines of the main and auxiliary blades; and the horizontal distance, represented as “ X ”, which is measured from the leading edges of the main and auxiliary blades. To facilitate the comprehension of the content, the vertical and horizontal distances relative to the blade chord are represented by the terms “ Y/C ” and “ X/C ”, which are designated as the vertical ratio and horizontal ratio, respectively. The forthcoming sections will scrutinize the auxiliary blade’s performance under varying pitch angles, and its vertical and horizontal positional attributes. In this simulation, the airfoil profile of the auxiliary blade is assumed to be identical to that of the main blade, i.e., NACA0021. In the present investigation, the control case is a Darrieus VAWT with a diameter of approximately 1 m. This rotor falls into the category of medium VAWTs; therefore, the geometrical modifications examined in this study can be applied to VAWTs with smaller rotor diameters without any challenge.

3. Governing Equations and Numerical Setup

3.1. Fluid Mechanics Equations

The URANS (Unsteady Reynolds-Averaged Navier–Stokes) equation is used to describe fluid flow dynamics around blades, allowing for an efficient and accurate analysis of unsteady, turbulent fluid flow behavior. The URANS equation is presented below [40]:

$$\frac{\partial \bar{u}_i}{\partial x_i} = 0 \quad (1)$$

$$\frac{\partial \bar{u}_i}{\partial t} + \bar{u}_j \frac{\partial}{\partial x_j} (\bar{u}_i) = -\frac{1}{\rho} \frac{\partial \bar{p}}{\partial x_i} + \frac{\partial}{\partial x_j} \left(\nu \frac{\partial \bar{u}_i}{\partial x_j} - \overline{u'_i u'_j} \right) \quad (2)$$

The terms \bar{u}_i (m/s) and \bar{u}_j (m/s) represent the mean components of velocity in the Cartesian system, defining the fundamental characteristics of flow physics. In contrast, the fluctuating velocities u'_i (m/s) and u'_j (m/s) are instrumental in capturing turbulence effects. Also, \bar{p} (N/m²), ρ ($\frac{\text{kg}}{\text{m}^3}$), and ν (m²/s) are the governing pressure, density, and kinematic viscosity of the fluid, respectively. The defining characteristic of $\overline{\rho u'_i u'_j}$ is the Reynolds stress, which represents the correlation between fluctuating quantities in velocity components. This property provides insight into the fluid’s intricate momentum transformations induced by turbulence.

3.2. Turbulence Modeling Equations

The Reynolds stress combines the intricate dynamics of the fluid flow around rotor blades. Hence, it is vital to determine a reasonable turbulence model for simulating fluid flow carefully. In solving turbulent flows, the $k - \varepsilon$ and $k - \omega$ turbulence models are typically employed, both of which are established on a set of two transport equations. The accurate modeling of turbulent flows is reliant on the successful solution of these equations. In essence, the use of an appropriate turbulence model is essential for ensuring the accurate simulation of fluid flow around blades. The selection of an appropriate model requires a comprehensive understanding of their respective strengths and limitations, as well as the contextual relevance of their intended application. An appropriate turbulence model is crucial for ensuring the precise fluid flow simulation around rotor blades. Selecting the most suitable model requires a thorough understanding of its individual strengths and limitations, as well as the contextual relevance of its specific application. The $k - \varepsilon$

model, widely utilized in CFD, is known for including empirical damping functions within the viscous sublayer. However, this characteristic compromises the model's accuracy in handling pressure gradients, particularly in the context of turbomachinery modeling [41]. As a result, using the $k - \varepsilon$ model is not advisable in specific scenarios. In contrast, the $k - \omega$ model serves as a viable alternative. This turbulence model does not necessitate damping terms and can reliably forecast flow behavior near surfaces. Nevertheless, its applicability in predicting turbulent flows in turbomachinery is limited due to its reliance on specific turbulence conditions, such as turbulence intensity. The shear-stress transport (SST) $k - \omega$ hybrid model was developed to address the inherent limitations of existing models. This approach integrates the $k - \varepsilon$ methodology to estimate flow in regions distanced from surfaces while concurrently leveraging the $k - \omega$ model to predict flow around blades [41]. In the framework of this model, turbulent kinetic energy (k) denotes the energy contained in turbulent eddies and vortices capable of generating turbulent motion. Additionally, the specific rate of the dissipation rate of kinetic energy (ω) quantifies the speed at which turbulent kinetic energy dissipates due to viscosity. The relations for k (m^2/s^2) and ω (s^{-1}) are presented below [42].

$$\rho \frac{\partial}{\partial t}(k) + \rho \nabla \cdot [k(\vec{u} - \vec{u}_g)] = \nabla \cdot \left[\left(\mu + \frac{\mu_t}{\sigma_k} \right) \nabla k \right] + G_k - Y_k \quad (3)$$

$$\rho \frac{\partial}{\partial t}(\omega) + \rho \nabla \cdot [\omega(\vec{u} - \vec{u}_g)] = \nabla \cdot \left[\left(\mu + \frac{\mu_t}{\sigma_\omega} \right) \nabla \omega \right] + G_\omega - Y_\omega \quad (4)$$

where Y_k ($\frac{\text{kg}}{\text{ms}^3}$) and G_k ($\frac{\text{kg}}{\text{ms}^3}$) represent the dissipation and generation of turbulence kinetic energy, respectively. Additionally, G_ω ($\frac{\text{kg}}{\text{m}^3 \cdot \text{s}^2}$) is the generation of ω , while Y_ω ($\frac{\text{kg}}{\text{m}^3 \cdot \text{s}^2}$) denotes ω dissipation. The turbulent Prandtl numbers for k and ω are denoted by σ_k and σ_ω , respectively. μ_t is the turbulent viscosity, computed from k and ω .

3.3. Turbine Mathematical Relations

The effectiveness of wind turbines can be determined through a mathematical analysis of the power and torque coefficients [43]:

$$C_p = \frac{P}{\frac{1}{2} \rho A V_\infty^3} \quad (5)$$

$$C_m = \frac{P}{\frac{1}{4} \rho D^2 H V_\infty^2} \quad (6)$$

where P ($\frac{\text{N} \cdot \text{m}}{\text{s}}$) denotes the total generated power of the turbine for revolutions, ρ ($\frac{\text{kg}}{\text{m}^3}$) is air density which is equal to 1.225 ($\frac{\text{kg}}{\text{m}^3}$), and V_∞ ($\frac{\text{m}}{\text{s}}$) is the wind velocity entering the rotor. The calculation of the rotor swept area in wind turbine design, A (m^2), is achieved by multiplying the diameter (D) and height (H). As that is a 2D simulation, the turbine height is considered equal to 1. An indispensable dimensionless parameter used in the design process is the tip speed ratio (TSR), which signifies the ratio of the tangential velocity of the blade tip to the incoming wind velocity. TSR is defined as follows [43]:

$$TSR = \frac{R\Omega}{V_\infty} \quad (7)$$

where Ω ($\frac{\text{rad}}{\text{s}}$) is considered as the rotor angular velocity and R (m) is the turbine radius.

Equation (8) establishes an analytical relationship between the azimuth angle and the angle of attack.

$$\alpha = \tan^{-1} \left(\frac{\sin \theta}{TSR + \cos \theta} \right) \quad (8)$$

where θ represents the azimuth angle, and α represents the angle of attack (AOA). In Figure 2, α is presented as a function of the azimuth angle for three selected TSRs.

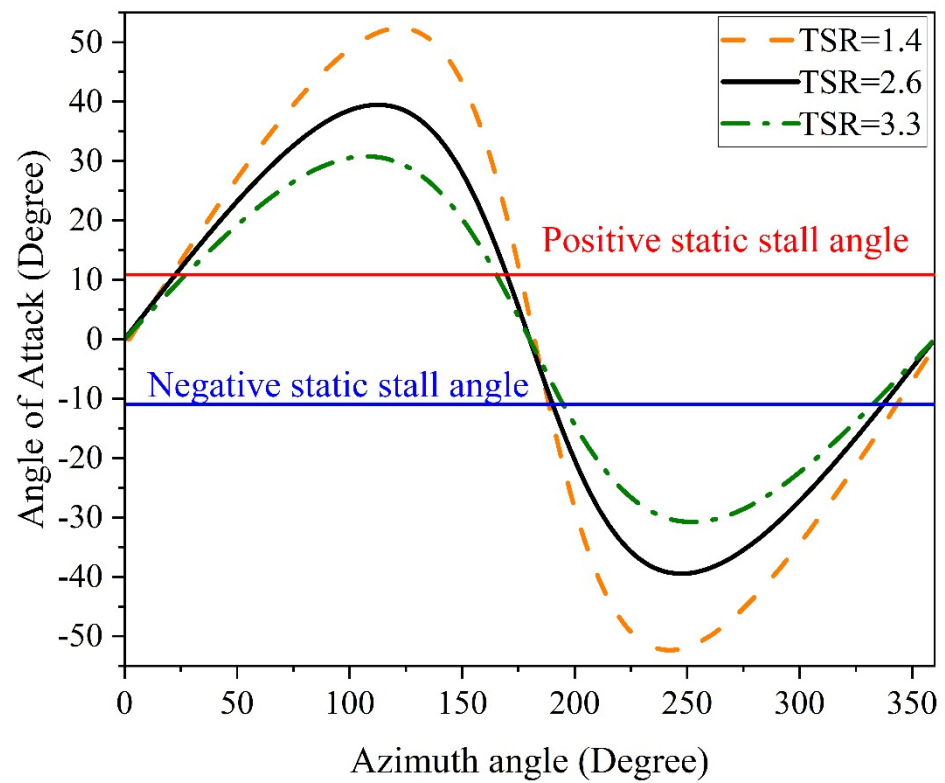


Figure 2. Theoretical AoA variation with azimuth angle for different TSR.

Based on the data presented in Figure 2, which illustrates the variation of AoA over a complete rotation, it is evident that the maximum and minimum AoA values exhibit an inverse relationship with the TSR, an indicator of angular velocity. With a decrease in TSR, the operational range of AoA expands, reflecting that alterations in the blade airfoil configuration yield more pronounced effects in the low-TSR range. This extended AoA range reduces the likelihood of stall occurrences, thus indicating improved performance. In other words, at low TSRs, when the rotor transitions from the downwind to the windward area, specifically when the azimuth angle is within the range of 300° to 360° , there is a sharp AoA. Under these conditions, the rotor achieves the negative static stall angle at a later point. Similarly, this phenomenon is observed during the transition of the blade from the upwind to leeward positions, where the azimuth angle spans from 140° to 200° . In these scenarios, rotor blades operating at lower TSRs experience a delay in reaching the positive static stall angle. C_l values are calculated using the following relations to determine the lift force based on rotor rotation and blade position changes, as shown in Figure 1c.

$$C_l = \frac{F_x \sin(\theta - \alpha) - F_y \cos(\theta - \alpha)}{\frac{1}{2} \rho A V_\infty^2} \quad (9)$$

The equation provided relates to the normal force F_y and tangential force F_x acting on the turbine blade. These forces were computed to determine the lift force based on the angles of attack and azimuth angle.

3.4. Computational Domain

In the current study, two-dimensional (2D) CFD simulation was used to examine the wake flow in the downstream region of the rotor. The 2D CFD approach was chosen because it has a proven ability to simulate wake flow accurately while minimizing computational

expenses [44]. The objective of this study was to minimize the influence of the lateral walls on the rotor's performance and flow development. An analysis of sensitivity was performed on three essential geometrical parameters to maintain a uniform fluid flow before and after the rotating zone. The following critical parameters are essential for this analysis: d_i , which represents the distance between the center of the rotor and the inlet and varies from $2D$ to $15D$; d_o , which means the distance between the center of the rotor and the outlet and ranges from $5D$ to $40D$; and the blockage ratio D/W , where " W " is the width of the computational domain. The sensitivity analysis results are illustrated in Figure 3. These findings suggest that adjustments to the stator's geometric specifications remarkably influence smooth fluid flow expansion and mitigate the impact of the walls on the turbine's performance.

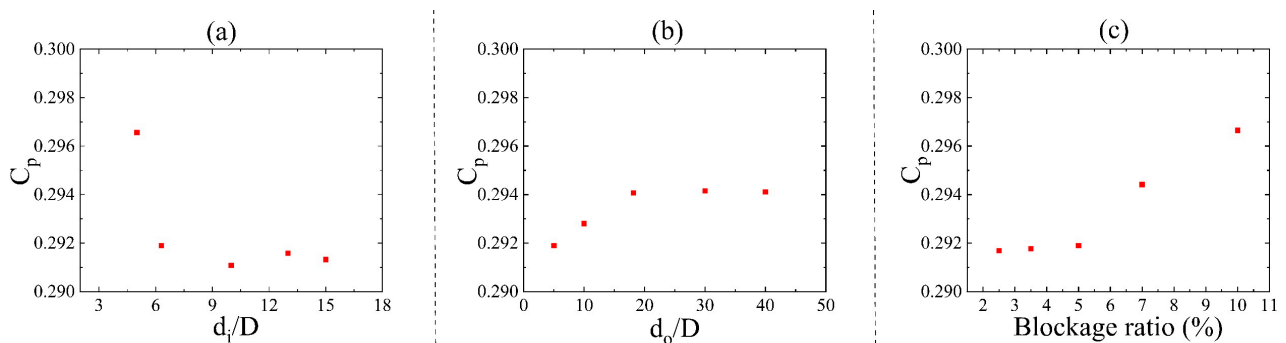


Figure 3. Computational domain sensitivity analysis: (a) inlet distance effect, (b) outlet distance effect, and (c) domain width effect [39].

Figure 3a shows that the calculated C_p for domains with inlet distances of $d_i = 2D$ and $5D$ tends to be overvalued. It is noteworthy that the difference in the calculated C_p between inlet distances of $d_i = 7D$ and $15D$ is insignificant, amounting to less than 1%. Hence, the recommendation is to opt for an inlet distance of $7D$ to alleviate the overestimation of C_p observed with smaller inlet distances. Figure 3b indicates that as d_o increases from $5D$ to $40D$, the variance in the value of C_p across different outlet distances progressively diminishes. Within this range, a mere 0.2% deviation is observed. Therefore, based on the analysis, it is advisable to consider $d_o = 20D$ as the optimal option to ensure an optimal flow expansion downstream of the rotor. As shown in Figure 3c, a blockage ratio of 10% leads to an overestimation of C_p due to flow acceleration or deflection [45]. A domain width of 20 times the rotor diameter is advisable, which translates to a blockage ratio of 5%. A schematic and dimensions of the domain can be seen in Figure 1c.

3.5. Boundary Conditions

In the present simulation, a constant wind velocity of 9 m/s ($Re = 740,000$) is prescribed at the inlet. To represent the wind stream's outflow into the atmosphere, a static gauge pressure of zero Pa is imposed at the outlet, given that the turbine domain exists at atmospheric pressure. Maintaining this boundary condition is imperative to ensure the validity and real-world applicability of the simulation results. Symmetry boundary conditions have been selected on the sides of the domain, as they are anticipated to exert a negligible impact on the outcomes. The non-slip boundary condition is applied to the turbine walls. To ensure authentic system simulation, it is compulsory to establish an association between the rotor and stationary fields using an interface boundary condition. Further, the mesh motion technique must accurately duplicate the system's rotation. An experimental investigation was accomplished in a low-speed wind tunnel with minimal turbulence intensity, and it was announced that this parameter corresponds to 5% at both the inlet and outlet boundaries.

3.6. Solver Settings

The ongoing investigation employs Ansys Fluent 2021 R1 software for numerical simulations. Considering the time dependency and unsteady flow around the blades, the transient method has been deemed appropriate. Moreover, due to air's incompressibility at low speeds, the pressure-based model has been chosen to solve the momentum and continuity equations. In order to attain high precision, we have incorporated the SIMPLE (Semi-Implicit Method for Pressure-Linked Equations) scheme for solving velocity–pressure-related issues. This pressure-based segregated algorithm effectively solves the momentum and pressure correction equations separately, making it a computationally efficient approach for simulating unsteady flow phenomena. The suitability of the SIMPLE algorithm is further augmented by the use of a fine mesh quality and small time-step size in this simulation. The second-order upwind algorithm is a robust method for discretizing various equations, including those governing the pressure, momentum, turbulence kinetic energy, and specific dissipation rate. The employed method demonstrates exceptional accuracy and efficiency in addressing related issues. In this simulation, convergence is initially determined by the C_m . As a universally applicable benchmark, the simulation is deemed to have converged when the difference between the torque coefficient values in two straight periods is less than 1% compared to those in previous periods. The convergence criteria for the x- and y- velocity components, as well as the continuity, k , and omega equations, have been defined with a threshold of 10^{-6} . To ensure compliance with these criteria, 30 iterations per time-step have been included in the process. This stringent methodology has been implemented to ensure that specified requirements are met and residuals remain below the designated threshold value. In this simulation, attention has been directed not only towards the convergence criterion but also towards the trends of torque fluctuations and output power derived from the solver. Specifically, until the torque and power fluctuations exhibit a consistent trend, the results of the turbine cycles are deemed invalid, indicating insufficient development and flow, as well as a lack of convergence in the solution. Once stability in the trend of the results is achieved, the power can be averaged to calculate C_p . Furthermore, it is only after the stabilization of oscillations that a rotor cycle is considered for evaluating the torque on a single blade.

3.7. Mesh Generation and Grid Independence Study

Picking a suitable mesh structure for the Darrieus VAWT is essential to capture intricate flow behaviors and sharp gradients near the airfoil surfaces while effectively managing computational costs. In this simulation, we employed ANSYS-Mesh for domain discretization. A fine, unstructured all-triangle grid with quadrilateral elements as the boundary layer mesh was used to optimize accuracy near the blade wall and avoid sudden flow jumps. Unstructured triangular elements were applied in both the rotating and stationary zones. We implemented gradual grid coarsening from the airfoil surfaces towards the interface of the rotation–stationary zones. The gradual increase in the size of the polyhedral triangular meshes approximates the prism meshes, which is a result of the boundary layer mesh developed around the airfoil, and has contributed to the accuracy and quality of the overall generated mesh. This approach has effectively prevented any abrupt transitions or sudden jumps in mesh size, ensuring a seamless integration between the boundary layer prism mesh and rotor triangular mesh. Moreover, the apex of each triangular element aligns precisely with the edges of the prism mesh associated with the boundary layer. The sliding interface was constructed using a non-conformal mesh with specific sizing, carefully designed to enhance grid density and improve flux calculation accuracy. The precision in generating an appropriate mesh to achieve accurate results for the secondary blade was also recognized. The mesh around the airfoil profile was set at 0.003 mm and featured 14 inflation layers with a growth rate of 1.15. It is important to emphasize that this study will impose a limit on the number of inflation layers used in the generation of the boundary layer mesh. The rationale for this limitation arises from the potential issues encountered when creating an excessive number of boundary layer meshes, particularly in scenarios

where the auxiliary blade is positioned close to the main blade. Such configurations may lead to interference among the meshes surrounding the blades, which could negatively impact mesh quality. To ensure the maintenance of high-quality results, reducing the number of boundary layers is necessary. To prevent a decrease in the number of inflations in the upcoming steps of the simulation, it is important to maintain a consistent mesh density and characteristics throughout the process. Therefore, starting with a smaller number of layers from the beginning is advisable, as this approach ensures the validity of the simulation. The detailed mesh distribution around the blades and rotor is shown in Figure 4. The mesh specifications for the rotor in the control case are presented in Table 2.

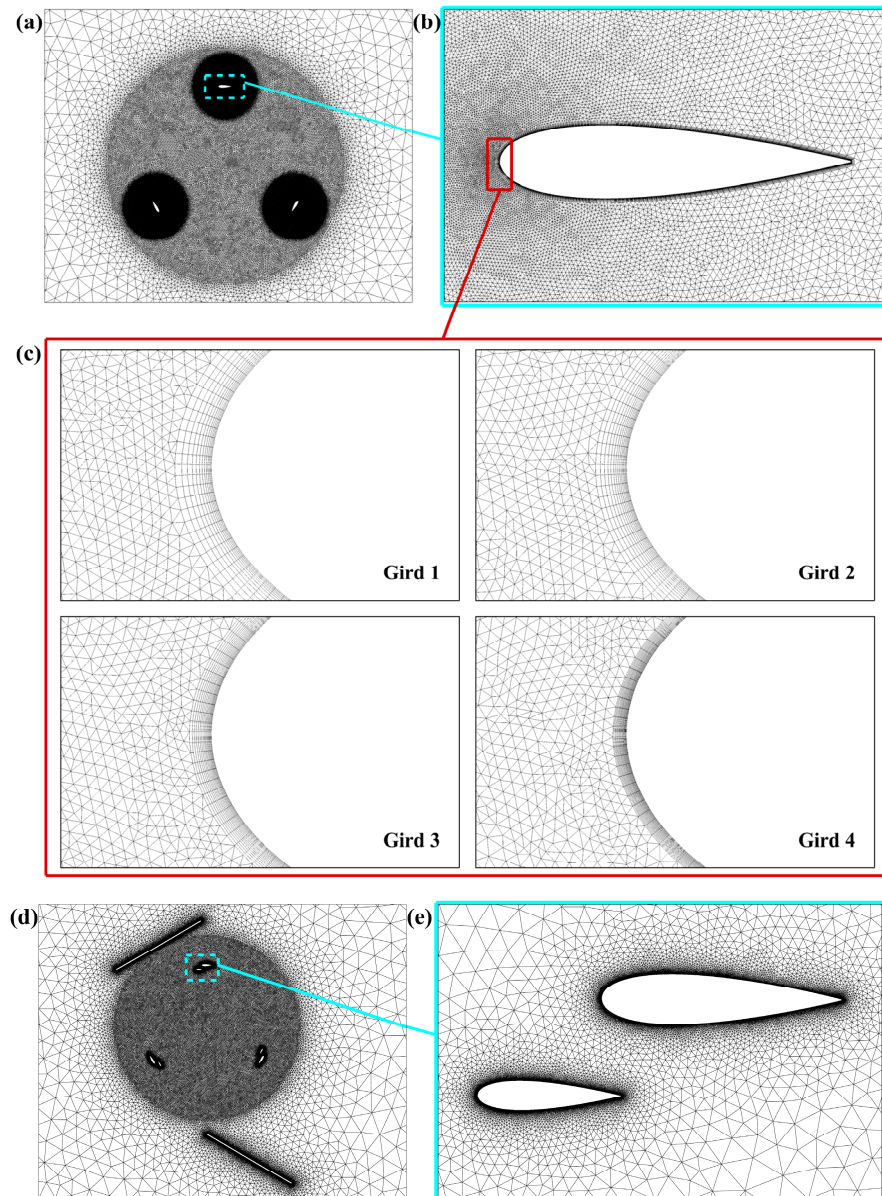


Figure 4. (a) Unstructured mesh around the Darrieus rotor for the control case, (b) mesh around single blade, (c) focused view of mesh levels around the leading edge, (d) unstructured mesh for modified rotor with auxiliary blades and double deflector, and (e) mesh around blade set.

Table 2. Grid independence summary [39].

Grid Properties	Grid 1	Grid 2	Grid 3	Grid 4
Number of elements $\times 10^3$	441	564	786	846
Airfoil element size (mm)	0.05	0.03	0.015	0.01
Number of inflation layer	12	14	16	18
First layer thickness (mm)	0.029	0.024	0.019	0.014
Inflation growth rate	1.2	1.15	1.1	1.05
Maximum skewness	0.946	0.979	0.969	0.984
Average Skewness	0.317	0.325	0.321	0.327
Averaged y^+	1.4	0.9	0.83	0.74
C_p	0.2918	0.2929	0.2939	0.2931

As illustrated in Figure 4c, a study was undertaken to ensure mesh independence for the conventional Darrieus rotor. Four distinct levels of mesh refinement were studied, characterized primarily by variations in grid size and density adjacent to the airfoil walls. The specific properties of each grid are detailed in Table 2, where Grid 1 denotes the coarsest grid, and Grid 4 denotes the finest.

The y^+ parameter is the primary determinant among the assessed meshes. y^+ conveys the dimensionless distance normal to the wall and scales with the boundary layer thickness, as represented in Equation (10) [46].

$$y^+ = \frac{\rho_w y u_\tau}{\mu_w} \quad (10)$$

The variable “ y ” denotes the normal length between the center of the grid and the blade surface. Here, ρ_w and μ_w depict the density and dynamic viscosity of air close to the blade surface, respectively. Friction velocity is defined as $u_\tau = \sqrt{\frac{\tau}{\rho}}$, where τ is the wall shear stress and can be estimated by $\mu \frac{\partial u}{\partial y}$. The boundary layer of the fluid flow can be categorized into distinct sublayers, precisely the laminar sublayer and the buffer layer. The laminar sublayer is represented by a y^+ range of $0 < y^+ < 5$, whereas the buffer layer is denoted by a y^+ range of $5 < y^+ < 30$. To accurately simulate the viscous sublayer using the SST k - ω turbulence model, utilizing a y^+ value around 1 is essential to confirm sufficient accuracy [47].

The y^+ contour plot highlights that the y^+ distribution around the blade airfoil profiles remains within an acceptable range, specifically around a value of 1. Notably, the y^+ value at the leading edge of the blade airfoil profile reaches a maximum of approximately 1, after which it decreases toward the trailing edge. Furthermore, as illustrated in Figure 5b, it is evident and precise that the y^+ values for all blades consistently fall within the acceptable range, with a maximum value of 1.02. This finding is in complete agreement with the contour plot presented. The maximum skewness values observed across various meshes indicated that they fell within an acceptable range of approximately 0.95, while the average skewness value was also within an acceptable range of about 0.33 [48]. It is important to highlight that Trentin et al. [49]. achieved a maximum skewness of 0.96 for the generated mesh featuring a triangular structure applied to a two-dimensional Darrieus VAWT that closely resembles the current turbine CAD model. In addition to the following verifications of the mesh study, the Grid Convergence Index (GCI) was assessed for various mesh cases, progressing from Grid 1, the coarsest configuration, to Grid 4, the finest configuration. According to Roache’s [50] relation applied to the GCI and utilizing a safety factor (F_s) of 1.25, $GCI_{coarse} = 5.1 \times 10^{-3}$ was determined for the coarse mesh, while $GCI_{fine} = 2.8 \times 10^{-3}$ was established for the fine mesh. These values correspond to 1.25% and 0.94% of the respective C_p for each mesh. After examining the C_p values in Table 2 and the C_m values for one blade in a full rotation of the rotor, shown in Figure 5, it can be concluded that varying the configuration and number of elements across the selected grids did not significantly impact the rotor’s output values. According to the C_p values outlined

in Table 2, Grid 3 demonstrates the highest value, while Grid 1 exhibits the lowest. The difference between the two is marginal, at less than one percent, indicating the accuracy of the solution and its independence from the number of meshes used.

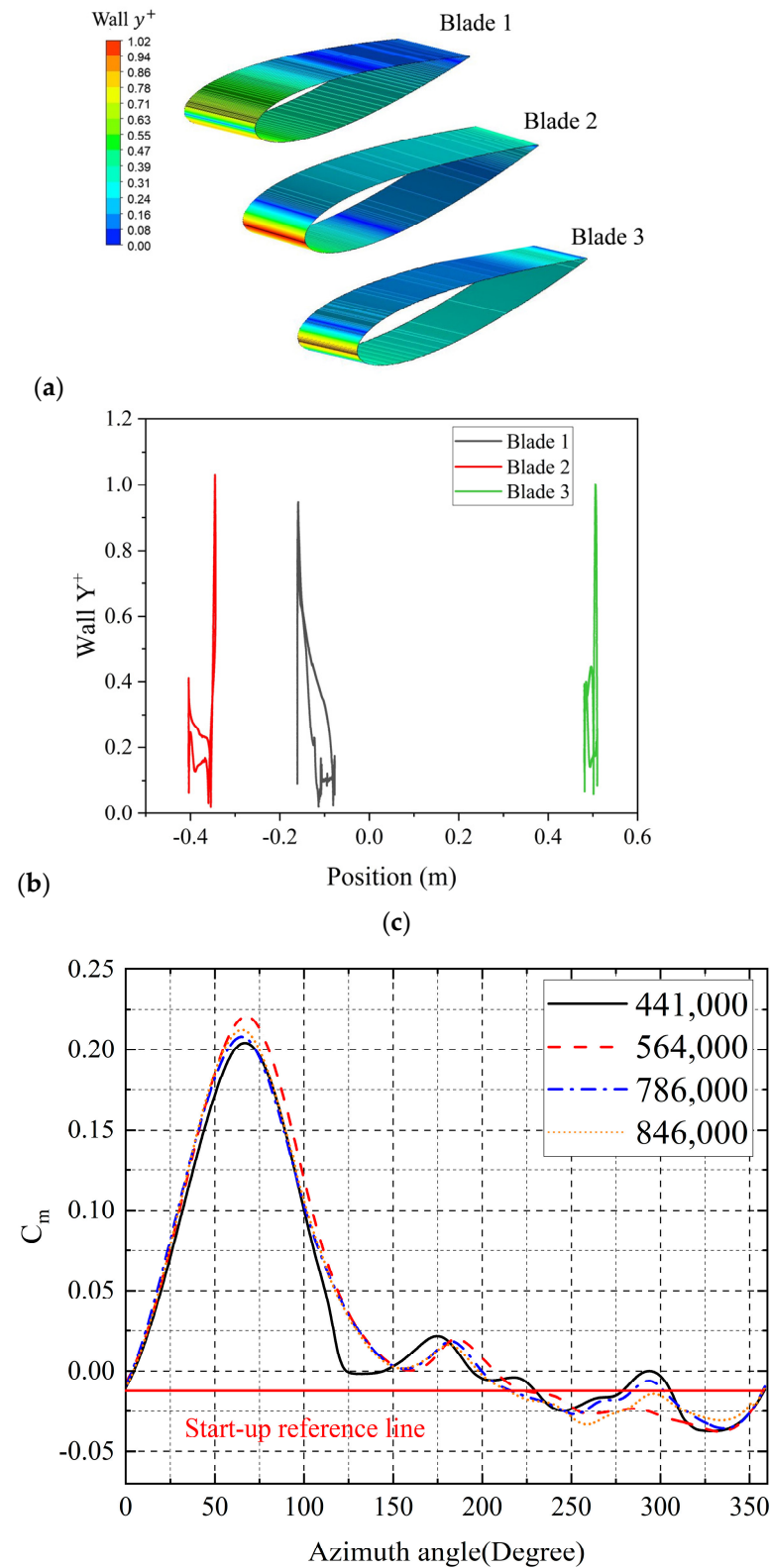


Figure 5. (a) Wall y^+ contour around the blades, (b) wall y^+ for Darrieus VAWT control case, and (c) one blade torque coefficient as a function of the azimuth angle in a complete rotation at $TSR = 2$.

3.8. Time-Step Independence

One of the primary challenges encountered in any CFD project is maintaining data stability at each cumulative time-step. This challenge is particularly significant for Darrieus VAWTs due to the sharp changes in airflow around the airfoils, especially at the low-TSR range, which contains a higher degree of fluctuation in vorticity gradients [51]. A comprehensive time-step study was conducted to establish the optimal simulation parameters for the Darrieus VAWT. The outcomes of the time-step investigation guided the final selection of parameters utilized in the subsequent simulation. This approach ensured that the simulation was executed with the most fitting configurations, thus enhancing the accuracy and dependability of the results obtained. In assessing the time-step, the Courant–Friedrichs–Lewy (C_{FL}) criterion, defined in Equation (11), was employed [52].

$$C_{FL} = \frac{(u \cdot \Delta t)}{\Delta x} \quad (11)$$

In the equation, u represents the peripheral velocity of the airfoil, Δt represents the time-step, and Δx represents the average distance between the centers of two cells on the airfoil. C_{FL} number measures are used to determine the relationship between the time increment Δt and the time taken by a fluid particle with a given velocity u to pass through a cell with dimension Δx . Equation (12) delineates the mathematical relationship between the time-step and the azimuth angle across varying angular velocities.

$$\Delta t = \frac{\Delta \theta}{\Omega \cdot \frac{180}{\pi}} \quad (12)$$

In the above mathematical calculation, which defines a correlation between the time-step size and azimuth angle, $\Delta \theta$ is denoted as the azimuth angle variations related to rotor rotation and Ω is the angular velocity.

In the context of viscous turbomachinery flows, utilizing a Courant number of approximately 10 is advisable to minimize errors [52]. Table 3 displays the C_{FL} numbers corresponding to various mesh cases and time-steps for two TSR values, 2 and 3.3, respectively. It is evident that varying time-step values are produced by assigning distinct $\Delta \theta$ for each angular velocity, as outlined in Equation (12). However, these differing time-steps are anticipated not significantly to affect the output data, such as the C_p . Additionally, the computation of the C_{FL} condition remaining within an acceptable range signifies the simulation's independence from the time-step, thereby ensuring the selection of an optimal time-step.

Table 3. C_{FL} for various spatial and temporal discretization [39].

TSR	Ω (rad/s)	$\Delta \theta$ (degree)	Δt (s)	Δx (mm)			
				2.5 Grid 1	2.1 Grid 2	1.7 Grid 3	1.3 Grid 4
				C_{FL}			
2	35.4	2	0.001	34	39.6	48.4	61.7
		1	0.0005	17	19.8	24.2	30.8
		0.5	0.00025	8.5	9.9	12.1	15.4
		0.1	0.00005	1.7	2	2.4	3
3.3	57.3	2	0.0006	32.6	36.92	45.3	57.61
		1	0.0003	16.3	18.5	22.6	28.8
		0.5	0.00015	8.4	9.2	11.3	14.4
		0.1	0.00003	1.7	1.8	2.2	2.9

Regarding Table 3, which shows that $\Delta \theta = 0.5^\circ$ is equivalent to $\Delta t = 0.00025$ for TSR = 2 or $\Delta t = 0.00015$ for TSR = 3.3, respectively, the Courant number decreases within

an acceptable range for Grid 1 and Grid 2. In light of the recent findings, it has been recommended that Grid 2 is selected, since Grid 2 has a finer mesh in comparison to Grid 1. To ensure an accurate simulation, it is imperative to select an appropriate time-step of $\Delta\theta = 0.5^\circ$. By adhering to these parameters, we expected to yield a reliable and precise simulation.

The graph depicted in Figure 6 displays C_m and its average values for Grid 2 in relation to the time independence analysis. The flow time was 0.2 s. The chart presents the results for four different time-step sizes: 0.001 s, 0.0005 s, 0.00025 s, and 0.00005 s. These time-steps correspond to $\Delta\theta$ of 2° , 1° , 0.5° , and 0.1° , respectively. The outcomes are according to the TSR value of 2.

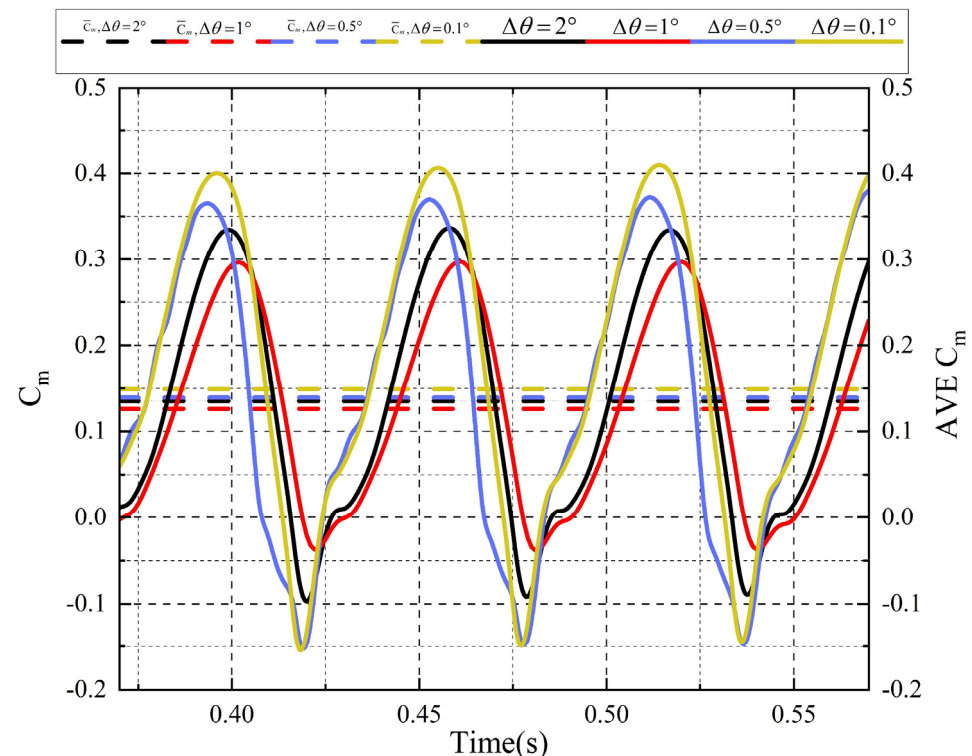


Figure 6. Variation of torque coefficient in relation to time for different time-steps and time-step sensitivity analysis at TSR = 2 [39].

In Figure 6, the alterations in C_m follow a consistent pattern across all measured time intervals. The data depicted in Figure 5 highlight that the variation in AVE C_m remains minimal across different time-steps, with a mere 1% relative difference observed as the angle changes from 0.1° to 1° .

After conducting a grid independence analysis, it was found that the changes in C_p were insignificant from Grid 2 onwards. As a result, this case was chosen for meshing. The time-step for the simulation should be selected based on $\Delta\theta = 0.5^\circ$, which led to a C_{FL} number lower than 10 in both evaluated TSRs. Therefore, this specific time-step is the primary time-step size for ensuring simulation accuracy in the subsequent process.

3.9. CFD Simulation Validation

Validation is conducted using the control case, against Castelli et al. [38], wherein both experimental and numerical results were presented. Furthermore, additional cases from previous CFD studies are introduced to assess the accuracy of the results and ascertain the trend depicted in the graphical representations. Notably, the absence of any reference to the blocking effect in the experimental study led to its exclusion from the CFD simulation. As aforementioned, an inlet boundary condition of $V = 9$ m/s ($Re = 740,000$) was used,

corresponding to the wind tunnel experiment. Validation was performed across eight TSRs spanning from 1.4 to 3.3. The validation results are visually depicted in Figure 7.

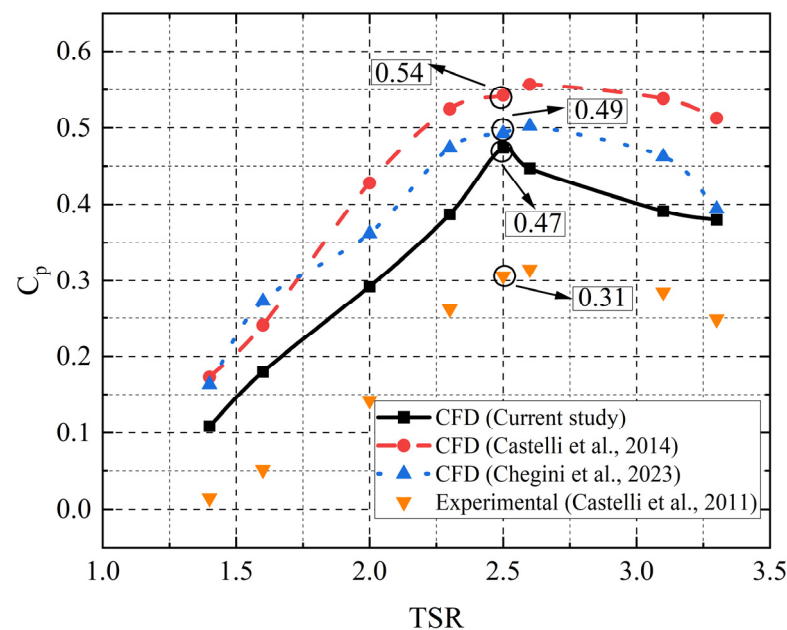


Figure 7. Comparison of Darrieus C_p from the present 2D simulation with experimental and CFD results [38,39,52,53].

In validating the precision of our current CFD study, we conducted a comprehensive comparison of our CFD results with the empirical data obtained by Castelli et al. [38] from their experiments and the numerical data presented by both Chegini et al. [53] and Castelli et al. [52]. Our CFD simulation exhibits comparable results with the empirical and previous CFD data, as depicted in Figure 7. Upon thorough examination, it is apparent that our current CFD findings demonstrate closer alignment with real-world scenarios and empirical data as opposed to the numerical results provided by Chegini et al. [53] and Castelli et al. [52]. The results from the recent CFD study conducted at a TSR = 2.5 indicate a C_p of 0.47. This value represents a deviation of 4% and 15% from the previous CFD results published by Chegini et al. [53] and Castelli et al. [52], respectively, demonstrating considerable agreement with their findings. Notably, a discernible disparity exists between the experimental data and all prior CFD outcomes. This variance can be attributed to the simplification of the 2D solution, utilization of a RANS-based model, and the exclusion of equipment-induced losses. Additionally, it is important to acknowledge that 2D simulations based on URANS methods are frequently favored in numerous CFD applications due to their cost efficiency. The limited errors associated with these simulations are often deemed acceptable due to their computational cost-effective advantages. The two-dimensional solutions were conducted on the mid-plane of the turbine, meaning that a single plane was traversed through the central section, effectively segmenting the turbine for analysis. Flow analysis was performed based on this mid-plane assumption, which provides an acceptable level of accuracy for vortex simulations. In other words, the two-dimensional simulations concentrate on the mid-plane of the Darrieus turbine, characterized by a substantial blade aspect ratio (height-to-chord ratio) of 16.97, thereby circumventing the involvement of three-dimensional tip impacts [54]. However, recent studies have demonstrated that the implementation of a superior-quality mesh has resulted in marginally improved outcomes when compared to the prior 2D URANS solutions. Furthermore, Ghafoorian et al. [39] have previously employed similar approaches in their CFD studies, validating the effectiveness of the 2D URANS methodology, with their results showing acceptable agreement with previous numerical and experimental studies.

The present CFD solution has been determined to be valid, as it satisfies the benchmarks established in the literature survey, mesh verification, and time-step studies. Consistent with graphical trends from prior CFD runs and experimental results, the current CFD solution demonstrates reliability.

4. Results and Discussion

This investigation analyzes the impact of three geometric parameters of the auxiliary blade pitch angle " β ", horizontal distance " X ", and vertical distance " Y ", on the conceptual design and aerodynamics of the rotor. The horizontal and vertical distances are measured relative to the leading edge of both the main and auxiliary blades.

4.1. Effect of Pitch Angle

The following section is dedicated to studying the impact of the auxiliary blade pitch angle on rotor aerodynamic performance. As depicted in Figure 1, the pitch angle, defined as the angle between the blade's chord and the rotor plane of rotation, has been varied within this section. It is evident that this variation in the auxiliary blade's position alters the angle of attack, which signifies the angle between the airflow and the blade's chord. Three values, namely 0° , 2° , and -5° , have been examined to assess the influence of the pitch angle on rotor aerodynamic performance and efficiency. In this phase, a pitch angle of 0° is designated as the baseline, with variations above and below this value analyzed to assess the impact of alterations in the pitch angle and optimization solution convergence. Concurrently, precautions were taken to prevent any unrealistic pitch angles from causing interference with either the leading or trailing edges of the main and auxiliary blades.

Figure 8 shows that adding an auxiliary blade to the rotor in the low-TSR range has led to both enhanced rotor efficiency and an expanded operating range, specifically extending the lower limit from 1.4 to 0.7. This extension indicates an improvement in the rotor's self-starting capability at a low-TSR range. The enhancement of the self-starting capacity, demonstrated by the increased efficiency and a broader operational range, reduces the initial torque required for the rotor to start functioning. A closer examination reveals that the pitch angle of the auxiliary blade significantly influences efficiency in the low-TSR range. Notably, positioning the auxiliary blade at a pitch angle of -5° results in a slight enhancement over the control case. Moreover, installing auxiliary blades at pitch angles of 0° and 2° leads to efficiency gains of 59% and 68% at $\text{TSR} = 1.4$, respectively. While installing the auxiliary blade at a pitch angle of 2° has shown better performance in the early TSRs, the performance of the auxiliary blade at a pitch angle of 0° has proven to be more impressive. Therefore, a pitch angle of 0° yielded the optimal performance. Evaluating pitch angles both above and below this baseline resulted in diminished performance. Consequently, it can be asserted that the solution has progressed toward convergence, lowering the necessity for the further examination of alternative pitch angle values. Incorporating an auxiliary blade within the high-TSR range did not improve the rotor's overall efficiency compared to the control case and led to a notable decrease in C_p values.

Figure 9 illustrates the static torque for the control case rotor and the cases with auxiliary blades during a complete rotation at $\text{TSR} = 1.4$. The results demonstrate that the inclusion of auxiliary blades has effectively enhanced the static torque. Particularly noteworthy is the substantial improvement in static torque observed when the auxiliary blades are set at pitch angles of 0° and 2° , compared to the scenario where the auxiliary blades are positioned at a pitch angle of -5° . These findings validate the performance map of the rotor in Figure 8, indicating that the modified rotor with auxiliary blades set at pitch angles of 0° and 2° exhibits a more significant increase in C_p compared to the control case rotor when the auxiliary blade is set at a pitch angle of -5° . The observed increase in static torque in one complete revolution of the modified rotor signifies an enhancement in the rotor's self-starting capability. This enhancement is particularly notable within azimuth angles ranging from 0° to 50° , with a marginal improvement, and becomes substantially prominent in the static torque increase between azimuth angles of 50° and 200° . While

the static torque of the rotor with an auxiliary blade set at a pitch angle of 2° exhibits a slightly higher increment compared to the 0° pitch angle auxiliary blade, the performance map of the rotor indicates a significant reduction in efficiency for the turbine equipped with the auxiliary blade at a pitch angle of 2° within the high-TSR range. Therefore, the configuration of the modified rotor with an auxiliary blade set at a 0° pitch angle is deemed the most favorable.

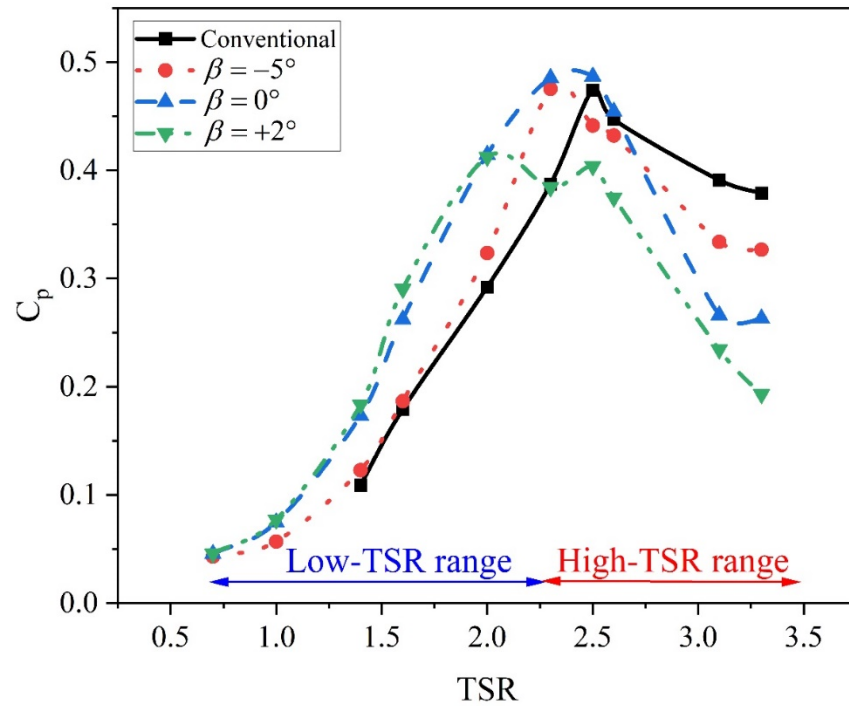


Figure 8. Effect of auxiliary blade pitch angle values on turbine C_p .

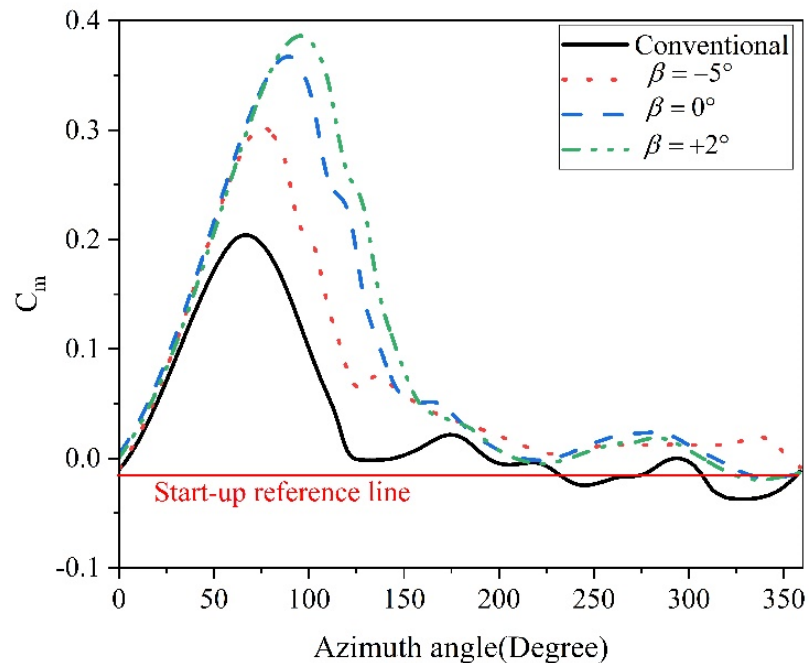


Figure 9. Variation of C_m over a complete rotation considering auxiliary blade with various pitch angles at $TSR = 1.4$.

In Figure 10, the pressure gradient distribution on the single blade of the Darrieus control case rotor is compared with that of a blade set of the modified Darrieus rotor with an auxiliary blade at a pitch angle of 0° . This configuration has been identified as the most efficient in enhancing the rotor's efficiency and self-starting capability. Notably, at an azimuth angle of 0° , where the blade is located at a windward area, the positive pressure distribution at the blade's leading edge is mainly identical for both configurations, and the negative pressure gradient on the pressure side does not exhibit significant differences. Consequently, the initial torque of the rotor equipped with an auxiliary blade does not significantly deviate from that of the conventional rotor. When the blades are in an upwind area, at an azimuth angle of 45° , the pressure distribution on both the suction side and pressure side in the modified rotor undergoes significant changes due to the rotor's rotation. Notably, a positive pressure gradient of approximately 150 Pa on the suction side of the auxiliary and main blades combines, resulting in increased static torque. The positive pressure gradient on the blade set positively increases the self-starting capability of the modified rotor in the upwind area, specifically at the low-TSR range. This combined positive pressure gradient on the blade suction side was absent in the control case rotor, which indicates the presence of the self-starting challenge for the conventional rotor. Conversely, on the pressure side, a negative pressure gradient of about -150 Pa leads to improved rotor rotation, indicating an enhanced self-starting capability. Moreover, the presence of the auxiliary blade at an azimuth angle of 90° enables the observation of the accumulation of positive and negative pressure gradients on the suction and pressure sides, respectively. At an azimuth angle of 135° , the presence of a positive pressure gradient on the suction side is not readily apparent, and its impact on enhancing the static torque has diminished. Conversely, a negative pressure gradient of approximately -130 Pa on the pressure side of the modified rotor fully envelops the blades, a contrast to the control case rotor where the pressure side is much more distant from the negative pressure gradient zone. The accumulation of the negative pressure gradient approximates the pressure side of the blade set and improves the modified rotor self-starting capability. As the rotor rotates towards the downwind area at azimuth angles of 225° and 285° , the pressure gradient distribution in both rotors becomes increasingly similar, leading to a reduction in the disparity of their static torques. The notable distinction lies in the presence of a negative pressure gradient of about -70 Pa on the trailing edge of the auxiliary blade on the pressure side of the main blade at an azimuth angle of 285° , which contributes slightly to the rotor's static torques and performance.

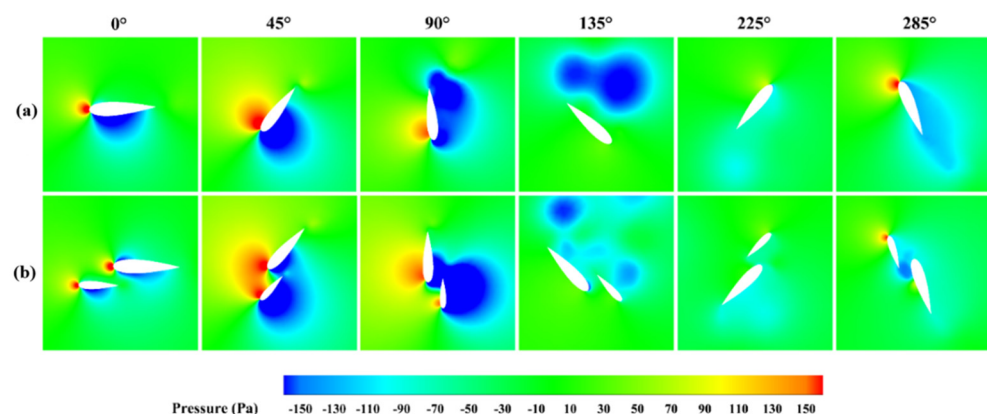


Figure 10. Pressure distribution for one blade set: (a) conventional Darrieus VAWT and (b) modified Darrieus VAWT with auxiliary blade at $\beta = 0^\circ$ for $TSR = 1.4$.

4.2. Effect of Horizontal Distance

This section assesses the impact of the horizontal distance between the auxiliary blade and the main blade on the rotor's aerodynamic performance and self-starting capability. The horizontal spacing is the distance between the auxiliary blade's leading edge and the

main blade's leading edge. In addition to the initial case, which has a horizontal distance of 44.2 mm, which is equal to the horizontal ratio of $X/C = 0.52$, two other horizontal distances of the auxiliary blade are examined: one with an increased distance from the main blade (61.3 mm) and the other with zero horizontal space (0 mm), which are equal to horizontal ratio values of 0.71 and 0. Positioning the auxiliary blade farther from the main blade places the trailing edge of the auxiliary blade ahead of the main blade. In contrast, bringing it closer to the main blade, the auxiliary blade's leading edge is aligned with the main blade. It should be noted that the pitch angle is assumed to be 0° based on the findings from the previous section, and based on the initial assumption, the vertical distance in this section is taken as 24.9 mm.

Based on Figure 11, it is evident that adjusting the horizontal distance between the auxiliary blade and the main blade has not notably impacted the turbine's efficiency or the self-starting capability of the rotor. This means that the expansion of the rotor's operating range from 1.4 to 0.7 did not change by this modification, and also that C_p values for all configurations at the initial TSRs were nearly identical. Moreover, repositioning the auxiliary blade in the low-TSR range failed to enhance the efficiency across all configurations. Notably, for configuration $X/C = 0$, the rotor's efficiency was similar to the control case and less than the initial modified rotor ($X/C = 0.52$); additionally, beyond $TSR = 2$, a sharp decline occurred, with C_p values lower than those of the control case rotor and the initial modified configuration. A similar trend was observed for configuration $X/C = 0.71$, where although the rotor's efficiency in the low-TSR range exceeded that of the control case, a significant drop occurred after $TSR=2$, persisting into the high-TSR range. The analysis revealed that, under the specified conditions of a pitch angle of 0° and a horizontal distance of 44.2 mm or $X/C = 0.52$, the displacement effect of the auxiliary blade did not significantly improve efficiency within the low-TSR range compared to the original modified rotor. In this section, an attempt was made to ensure the convergence of the study results by evaluating values both above and below the baseline. It was determined that neither increasing nor decreasing the horizontal distance of the auxiliary blade from the main blade enhances rotor efficiency. Furthermore, at the high-TSR range, this adjustment led to a significant reduction in efficiency. Consequently, there is no further necessity to examine horizontal distances, as the outcomes of the parametric study have demonstrated convergence. Therefore, it has been determined that the initial modified rotor configuration remains the most optimal configuration.

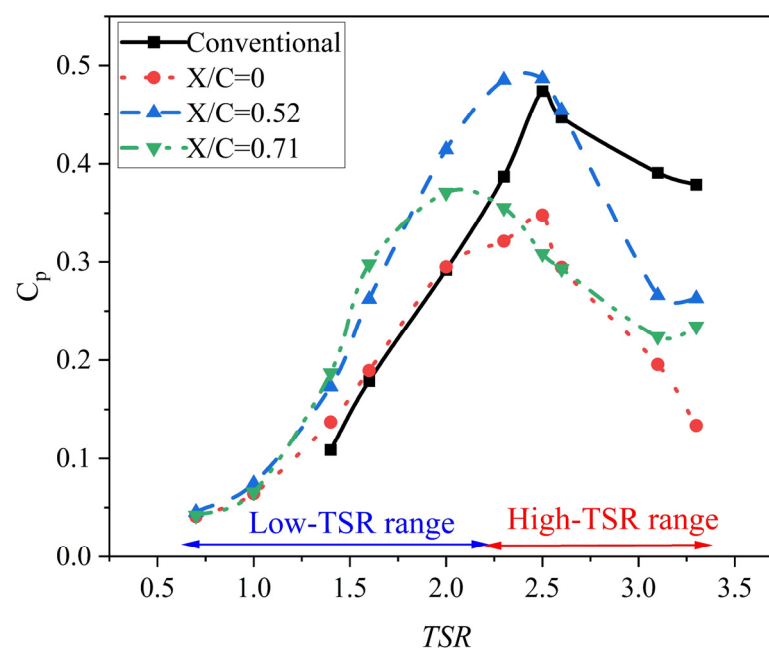


Figure 11. Effect of auxiliary blade horizontal distance on turbine C_p .

The findings depicted in Figure 12 reveal that the static torque of a modified rotor blade set, within the initial azimuth angles ranging from 0° to 50° , exhibits little deviation from that of the control case rotor. However, a substantial enhancement in the static torque, and consequently the self-starting capability of the rotor, becomes prominent within the azimuth angle range of 50° to 200° . Furthermore, the comparatively lower improvement of C_m values for the modified rotor with $x = 0$ mm, in contrast to the other two modified configurations, corroborates the precision of the performance map results, which indicated that the C_p value of this configuration is lower than the two other modified configurations at $\text{TSR} = 1.4$. The static torque of the modified rotor with $X/C = 0.71$ exceeds that of the initial modified configuration with $X = 44.2$ mm or $X/C = 0.52$ by a small margin. However, based on the performance map of the rotor, it is evident that the modified rotor with $X/C = 0.52$ demonstrates higher efficiency in the low-TSR range and experiences lower efficiency loss in the high-TSR range compared to the control case rotor. These points serve as compelling evidence for the superior performance of the initial modified rotor.

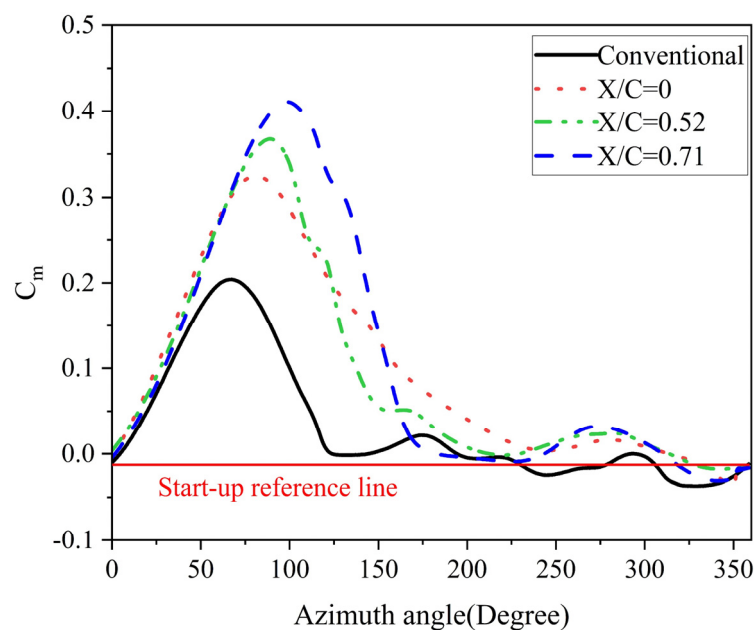


Figure 12. Variation of C_m over a complete rotation considering auxiliary blade with various horizontal distances at $\text{TSR} = 1.4$.

4.3. Effect of Vertical Distance

In this section, we will assess the vertical distance between the chord of the auxiliary blade and the main blade. Specifically, we will examine the closest vertical distance to the main blade, which measures 19.9 mm or $Y/C = 0.23$, and two longer vertical distances of 34.9 mm ($Y/C = 0.41$) and 49.9 mm ($Y/C = 0.58$) compared to the initial vertical distance of 24.9 mm, which is equal to the vertical ratio of 0.29. Based on the optimal design parameters outlined in the preceding two sections, this section sets the pitch angle to 0, and the horizontal distance measures 44.2 mm or the horizontal ratio of 0.52. In contrast, the vertical distance is the focal point for determining the optimal value.

Based on the data presented in Figure 13, the proximity of the auxiliary blade to the main blade has resulted in a minor decrease in the efficiency of the modified turbine compared to the initial modified rotor within the low-TSR range, impacting its self-starting capability. Conversely, an indiscriminate displacement of the auxiliary blade has also led to a marginal decrease in efficiency. Notably, positioning the auxiliary blade at $Y = 34.9$ mm, which is equal to $Y/C = 0.41$, has enhanced rotor efficiency compared to the configuration with the auxiliary blade at $Y/C = 0.29$. However, relocating the auxiliary blade to $Y/C = 0.58$ has caused a slight drop in efficiency compared to the configuration with the

$Y/C = 0.41$ auxiliary blade position. Furthermore, the modified rotor with the auxiliary blade at $Y/C = 0.58$ has led to a notable performance decline within the high-TSR range compared to other configurations. At this stage, the vertical distance of 19.9 mm or $Y/C = 0.23$ resulted in the auxiliary blade being positioned too close to the main blade, significantly reducing the efficiency in the low-TSR range compared to the baseline ($Y/C = 0.29$). This reduction was also observed within a portion of the high-TSR range. Consequently, examining vertical distances below this threshold is not logically necessary. Regarding the increase in vertical distance values, it was noted that with each incremental increase in vertical distance, C_p values exceeded those of the baseline across most TSR ranges. However, when the vertical distance was further increased to $Y = 49.9$ mm or $Y/C = 0.58$, a marked decline in C_p was observed. Therefore, $Y = 34.9$ mm, which is equal to $Y/C = 0.41$, was identified as the optimal configuration. The optimal mode was established, and the results appeared to converge consistently. Also, the modified turbine with an auxiliary blade at $Y/C = 0.41$ performed 40% better than the modified rotor with an auxiliary blade at $Y/C = 0.23$ at $TSR = 1.4$. Therefore, it has been determined to be the most optimal configuration for the modified rotor with an auxiliary blade. It is significant to note that the incorporation of an auxiliary blade in each configuration and installation position has enhanced the operational range of the rotor within the low-TSR range from 1.4 to 0.7. Specifically, the C_p value for the conventional rotor at TSR values less than 1.5 was nearly zero, indicating the turbine's inefficiency, a finding consistent with the research conducted by Mohamed et al. [14]. In contrast, the modified rotor equipped with an auxiliary blade achieved a C_p value of approximately 0.5 at the lowest TSR, thereby demonstrating an improvement in the rotor's self-starting capability and overall performance compared to the conventional design.

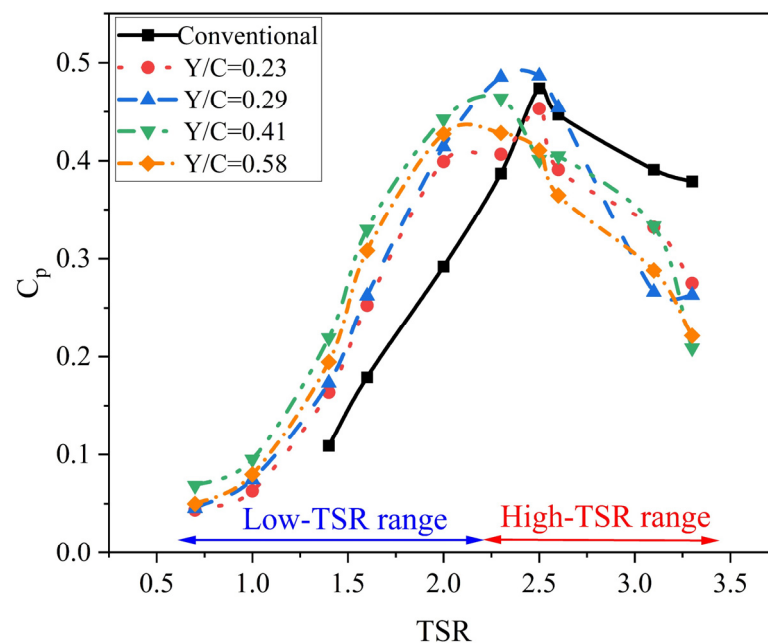


Figure 13. Effect of auxiliary blade vertical distance on turbine C_p .

In Figure 14, the optimized rotor with auxiliary blades positioned at varying vertical distances did not demonstrate a notable improvement in static torque within azimuth angles ranging from 0° to 50° . However, it highlighted enhanced C_m values and subsequently improved the self-starting capability, predominantly within azimuth angles of 50° to 200° . Furthermore, it is evident that the C_m values for the modified rotor with the auxiliary blade at a vertical ratio of $Y/C = 0.41$, at azimuth angles of 50° to 100° , exhibited only a slight margin in comparison to the C_m values obtained for the modified rotor with the auxiliary blade at $Y = 49.9$ mm or $Y/C = 0.58$. These results substantiate the enhanced C_p values of

this configuration within the performance map. Based on the performance map analysis of the turbine under various configurations and the assessment of static torques, which are the criteria for self-starting capability evaluation, it has been determined that the most efficient rotor requiring minimal initial torque for the starting operation and optimum self-starting capability is a modified rotor with an auxiliary blade. This optimal configuration involves a pitch angle of 0° and a horizontal and vertical position of 44.2 mm and 34.9 mm, which correspond to $X/C = 0.52$ and $Y/C = 0.41$, respectively.

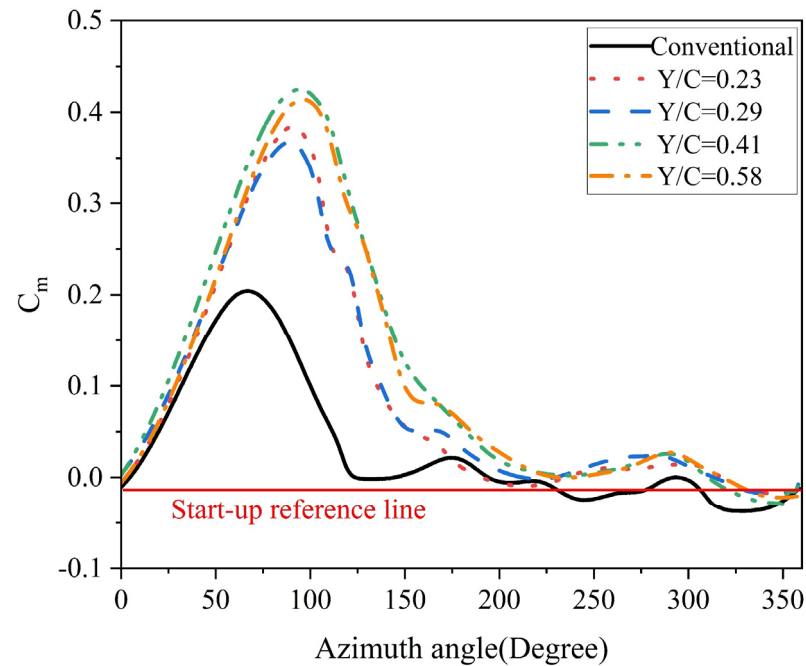


Figure 14. Variation of C_m over a complete rotation considering auxiliary blade with various vertical distances at $TSR = 1.4$.

Figure 15 shows the velocity field for the control case rotor and the optimized modified rotor at $TSR = 2.6$ within the high- TSR range where the rotor efficiency declined. It is evident that the impact of the auxiliary blade is highly discernible on the flow physics and wake flow behind the rotor and blades. Upon conducting a detailed analysis, it is evident that the wake flow downstream of the optimized modified rotor is more intense compared to the control case rotor. This is due to the distribution of the low-velocity area in the space between the blades and behind the rotor. Additionally, the wake flow is substantially developed along the trailing edge of the main blade, which is not observed in the control case rotor. The presence of the auxiliary blade significantly influences the extension and development of the wake flow behind the main blade. It is essential to highlight that the efficiency of the optimal modified rotor with the auxiliary blade diminishes only at high rotational speeds within the high- TSR range, due to the formation of a swirling flow on the suction side of the auxiliary blade. This swirling flow leads to flow separation and adversely affects aerodynamic performance, as this swirling flow happens in a minimal gap between the blade set. Conversely, based on the performance map in the low- TSR range, the modified rotor demonstrates enhanced performance and improved self-starting capability, indicating the negative impact of swirling flow and flow separation, which are observed only in the high- TSR range. Additionally, it is crucial to consider the adverse effect of blade-to-blade interaction in the case of the optimized modified rotor at the high- TSR range. This interaction occurs when rotor blades are in close proximity, resulting in adverse effects from the swirling or wake flow on neighboring blades [55]. Such interactions can disrupt aerodynamic performance and reduce overall efficiency, specifically in the high- TSR range, aligning with observations from the performance map and reinforcing its validity.

In other words, within the low-TSR range, the swirling flow in the confined gap between the primary and auxiliary blades does not worsen the adverse effects of blade-to-blade interaction and remains imperceptible. Not only does it avoid disrupting the aerodynamic performance, but it also aids in improving efficiency.

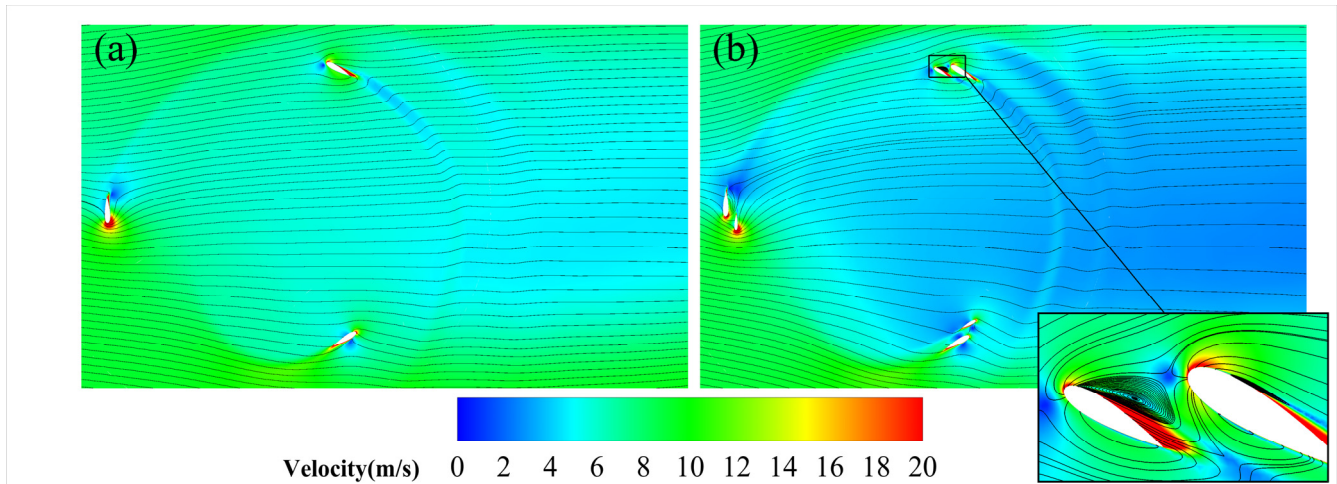


Figure 15. Velocity contour plot for (a) conventional rotor and (b) optimum modified rotor with auxiliary blade at $TSR = 2.6$ and $\theta = 90^\circ$.

Based on the vorticity contour presented in Figure 16, it can be observed that the negative vorticity along the suction side of the blades extends from the leading edge to the trailing edge. This developed negative vorticity signifies the presence of swirling flow and subsequent flow separation. When the blade set transitions from the downwind region to the windward area, the auxiliary blade, positioned at a steep AoA around -20° , creates noticeable negative vorticity on its suction side as it enters the windward section at an azimuth angle of approximately 340° . The proximity of this angle of attack to the negative static stall angle, approximately -13° , indicates an increased risk of blade stalling, leading to reduced rotor efficiency. The negative vorticity is formed only on the main blade in the conventional rotor. When the blade is positioned at an azimuth angle of approximately 340° and experiences a steep AoA of about -20° , there remains a potential for stall phenomena. In this scenario, the negative vorticity is localized to one blade. However, in modified turbine designs, the negative vorticity and subsequent swirling flow develop on two blades, thereby resulting in reduced efficiency for this configuration when compared to conventional rotors, particularly in high-TSR conditions. Figure 16c can verify the vorticity field and the stall occurrence in the case of an azimuth angle of 340° . It is evident that the lift force of the optimized rotor with the auxiliary blade in the azimuth angle range of 250° to 360° experiences a significant decrease in comparison to the control case. This phenomenon is further supported by Figure 16d, which indicates a noteworthy drop in lift force at the angle of attack of -20° , which is associated with an azimuth angle of 340° . This reduction in lift force at this angle clearly indicates the adverse effects of stall. However, the lift force at the initial azimuth angle, particularly in the 0° to 50° range, resulted in negative C_l values for the control rotor. In contrast, the optimized rotor, equipped with an auxiliary blade, exhibited higher C_l values, indicating an enhancement in the rotor's self-starting capability with auxiliary blades. It is important to highlight that this simulation is conducted at $TSR = 2.6$, which falls within the high-TSR range. According to Figure 2, not only is the AoA range reduced, but the blade also experiences a static stall angle at an earlier point. This phenomenon is a contributing factor to the decline in rotor performance within the high-TSR range, which subsequently elevates the likelihood of stall occurrences. Stall results in a sudden reduction in the blade lift force when the angle of attack increases from downwind to windward or upwind to leeward as it happened for

the modified rotor with auxiliary blades. When the stall is detected at an angle of attack of -20° and an azimuth angle of 340° , it causes a decrease in C_l beside the occurrence of flow separation and swirling flow between the main and auxiliary blades, as well as negative vorticity. These effects have a destructive impact on the aerodynamics of the modified rotor. The simultaneous presence of swirling flow, flow separation, and negative vorticity in the restricted gap between the blades worsens the adverse effects of the blade-to-blade interaction. In contrast, conventional rotors do not exhibit the blade-to-blade interaction phenomenon. Consequently, these rotors exhibit superior performance in high-TSR ranges and under conditions where the performance of rotors equipped with auxiliary blades has declined.

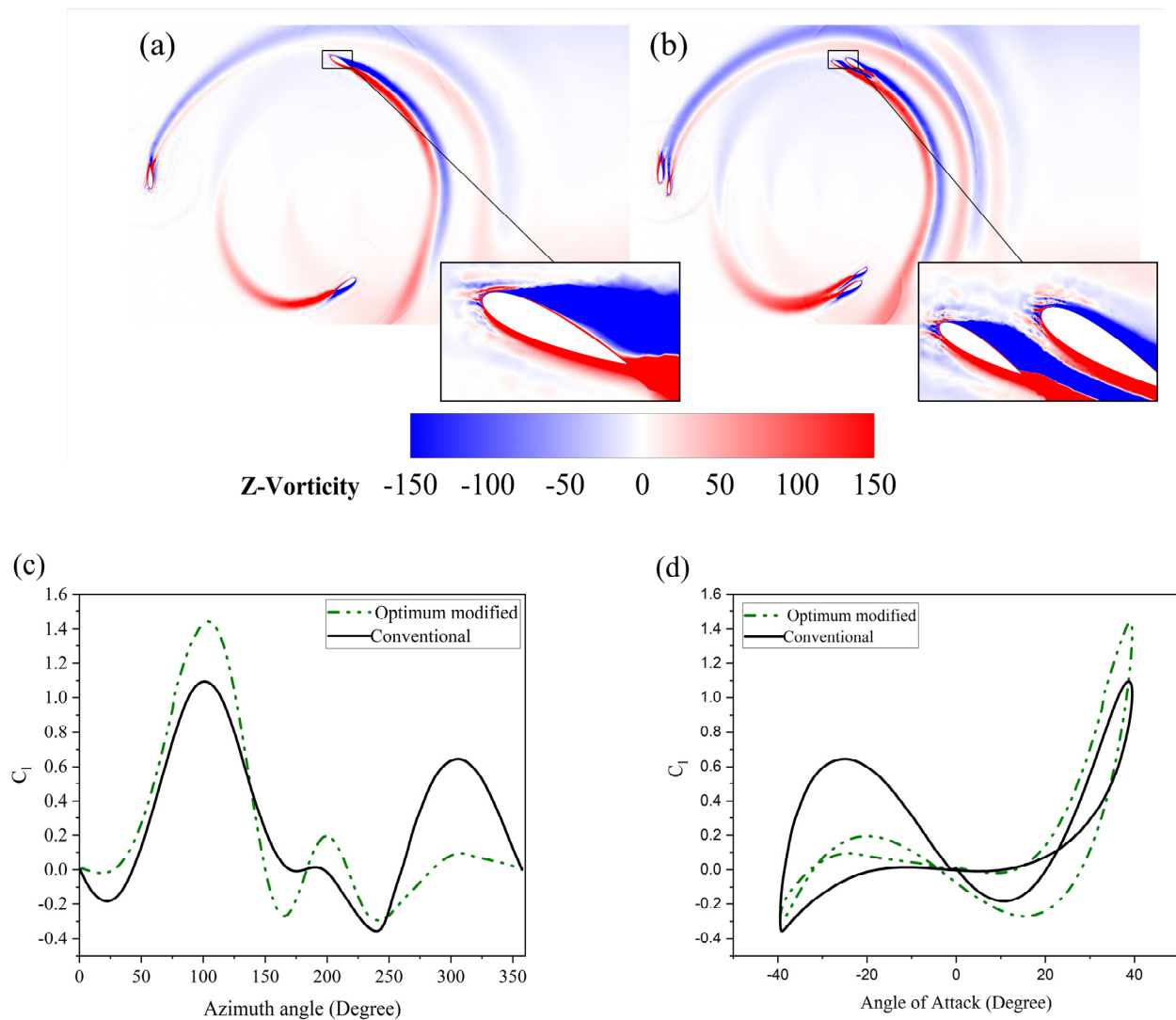


Figure 16. Z-vorticity contour plot for (a) conventional rotor (b), optimal modified rotor with auxiliary blade at $TSR = 2.6$ and $\theta = 90^\circ$, (c) lift coefficient variation over a complete rotation, and (d) lift coefficient variation as a function of AoA.

4.4. Effect of Deflector Installation

Next, we added a deflector to the modified rotor that has auxiliary blades. The reason for this design is that adding the auxiliary blades only improved the rotor efficiency at the low-TSR range and initial torque, resulting in self-starting capability enhancement. However, it caused a decrease in the rotor's efficiency at the high-TSR range. By installing the deflector, we aim to improve the rotor's efficiency at the high-TSR range. Deflectors are situated in three distinct configurations: double deflector, top deflector, and bottom

deflector, as depicted in Figure 1. The impact of incorporating each deflector arrangement on the modified rotor performance was investigated through its performance map and an analysis of the flow field.

Based on Figure 17, it is evident that the deflector installation in each configuration successfully increased the operating range of the rotor in the low-TSR range. However, the installation of a single top deflector negatively affects the efficiency of the modified rotor in the low-TSR range; specifically, the top deflector resulted in a 71% decrease in C_p at TSR = 1.4 compared to the case of the bottom deflector. Also, it was observed that using a single bottom deflector gained a small margin in the low-TSR range compared to employing a double deflector. It was noted that within the high-TSR range, the double deflector configuration significantly enhanced the efficiency of the modified rotor, a crucial factor in turbine performance compared to other configurations. Overall, installing a deflector in any configuration significantly increased the turbine's efficiency in the high-TSR range compared to both the control case and the modified rotor. The installation of a double deflector at a TSR = 2.5 resulted in an increase in C_p to 0.69, representing a 47% enhancement in C_p compared to the control case, which was calculated at about 0.47 at the same TSR. In contrast, the rotor equipped with an auxiliary blade without a deflector at the same TSR = 2.5, which operates within the high-TSR range, recorded a C_p value of approximately 0.4. This indicates that the rotor with the double deflector has achieved a 73% improvement in efficiency relative to the modified rotor with the auxiliary blade. This significant enhancement in rotor performance at elevated TSR values underscores the effectiveness of the deflector in mitigating the inefficiencies associated with the auxiliary blade-modified rotor within this operational range.

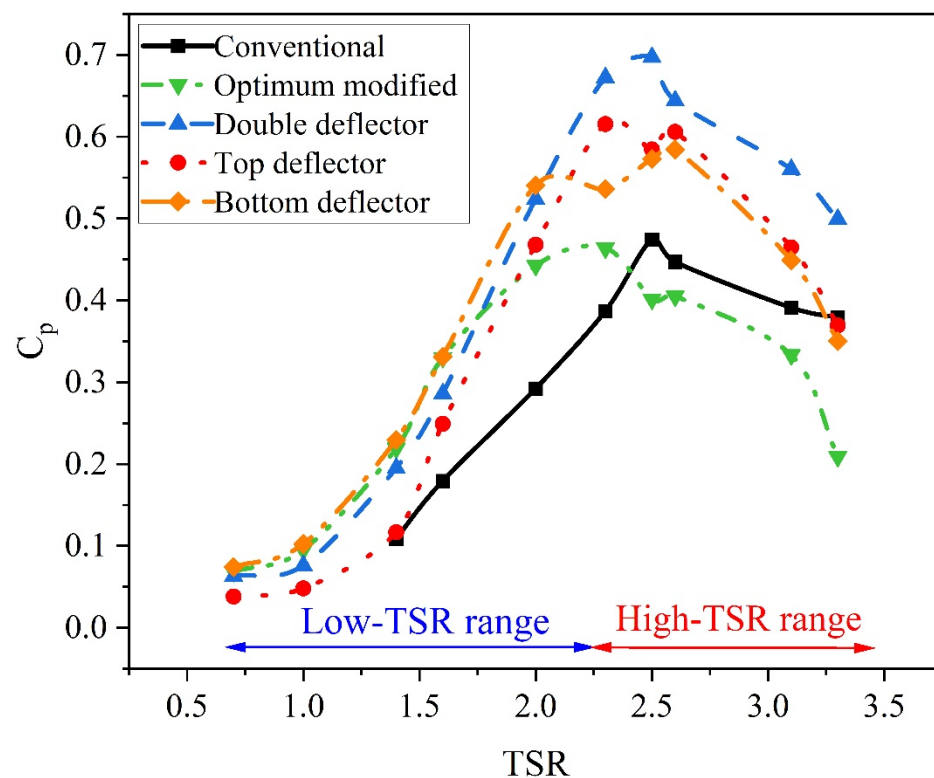


Figure 17. Effect of deflector installation on turbine C_p .

From Figure 18, it is evident that the rotor, when lacking a deflector, exhibited a wake flow, resulting in a more pronounced low-velocity region between the blades and downstream of the rotor. Therefore, deflector installation led to a reduced likelihood of low-velocity zone formation around the rotor blades. Notably, a TSR of 2.6, falling within the high-TSR range, indicates the presence of an approximate velocity of 20 m/s

on the suction side of the auxiliary blade under all conditions. This velocity profile can potentially exacerbate aerodynamic performance and blade-to-blade interaction through swirling flow, resulting in flow separation at a high-TSR range. However, implementing a deflector around the rotor has effectively mitigated the adverse effects of swirling flow, flow separation, and blade-to-blade interaction to a significant extent. This is evidenced by the restriction of swirling flow to an acceptable level on the suction side of the auxiliary blade, as depicted by the streamline and swirling flow comparison in Figure 18(a₁,b₁). Implementing a deflector to mitigate rotor efficiency loss has proven successful, effectively maintaining rotor aerodynamic performance within the high-TSR range. Notably, the design of the double deflector has demonstrated greater efficacy in enhancing rotor aerodynamic performance and efficiency. This design restricts the swirling flow on the auxiliary blade's suction side to a greater extent than other configurations, indicating a delayed flow separation. In rotors equipped with auxiliary blades, it is noteworthy that when the blade set is positioned in the windward direction with a high angle of attack, the region with a high tangential velocity remains observable on the suction side of the auxiliary blade. This phenomenon persists despite the presence of a deflector, and the reduction in the swirling flow on the suction side of the auxiliary blade is the only enhancement that occurred by the deflector installation.

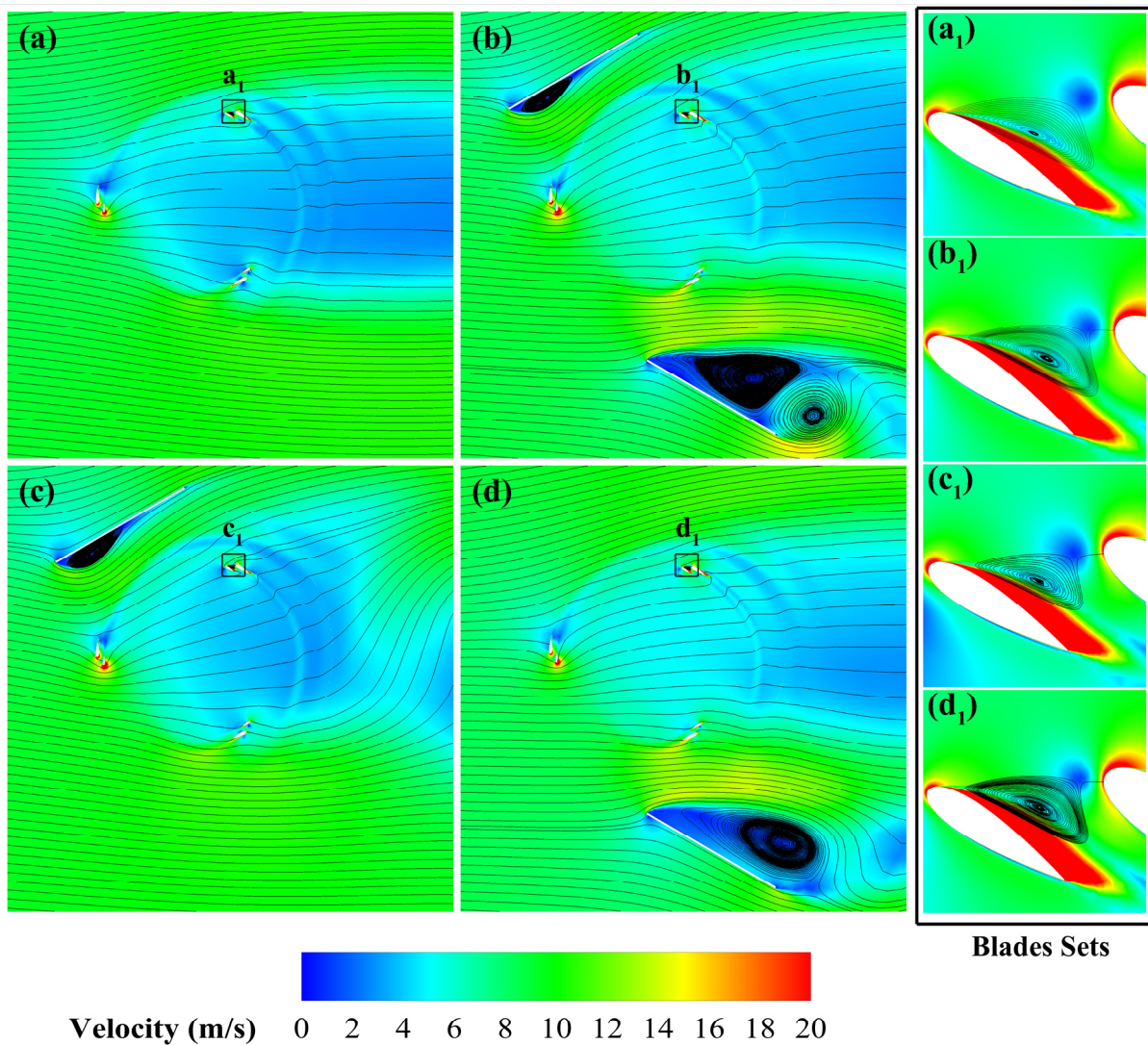


Figure 18. Velocity contour plot for (a) optimum modified rotor, (b) double deflector, (c) top deflector, (d) bottom deflector and (a₁–d₁) Detailed view of the flow field for blade set at TSR = 2.6 and $\theta = 90^\circ$.

The analysis depicted in Figure 19 illustrates the generation of a negative vorticity on the suction side of the auxiliary blade. This vorticity develops from the leading edge to the trailing edge. The negative vorticity on the suction side of the auxiliary blade at the limited gap between blade sets raises concerns regarding potential flow separation and an unfavorable blade-to-blade interaction at this high-TSR range value. On the contrary, the positioning of the blade set in the windward area, within the critical angle of the attack range of approximately -20° and azimuth angle of 340° (as shown in Figure 2), nearing the static stall angle, is likely to promote blade stall and disrupt aerodynamic performance. The observation of the formation of a negative vorticity on the suction side of the auxiliary blade supports this. The findings in Figure 19e imply that within the azimuth angle range of 300° to 360° , where the aforementioned blade is situated in the windward region, the lift force of the modified blade with the auxiliary blade has experienced a loss in C_l ; however, any deflector configuration has an enhanced lift. This underlines the potential of deflector installation as a viable approach to mitigate stalling in these conditions and to improve rotor performance. Figure 19f further supports the findings above, indicating that rotors with deflectors exhibit a higher C_l value at an AoA equivalent to -20° . Additionally, it is evident that during the initial azimuth angles ranging from 0° to 50° , wherein the blade set was positioned in the windward and upwind regions, the presence of the deflector did not contribute to an improvement in C_l . This supports the deflector's inefficacy in the low-TSR range, underscoring the validity of the turbine's performance map. The deflector effectively directs the flow and generates the vorticity in an appropriate direction, thereby reducing the likelihood of dynamic stall when the blade set transitions from the downwind to the windward region, where the angle of attack is sharp and approaching the static stall angle. Deflector installation is imperative to avoid the abrupt reduction in the blade set's lift force, which is an adverse impact of dynamic stall, as observed in the modified rotor that lacks a deflector. Also, looking at vorticity around deflectors, the deflector positioned at the top of the rotor has induced a positive vorticity, causing the swirling flow to adopt the counter-clockwise direction at the deflector's tip, aligning with the rotor's counter-clockwise rotation. This alignment has notably enhanced the rotor's torque and efficiency.

Upon analyzing Figure 20, it is evident that the pressure distribution in the leading edge and the pressure and suction sides remain nearly identical for both rotors, with or without deflectors. However, at an azimuth angle of 45° , it is observed that the pressure disparity between the suction and pressure sides of the rotor equipped with a double deflector has intensified. This has led to a more widespread negative pressure difference of approximately -150 Pa on the pressure side of the double deflector-equipped rotor, signifying an increase in torque within this region and an enhancement in the turbine's efficiency. Furthermore, the extensive distribution of the -150 Pa pressure difference on the pressure side of the blade set associated with the double deflector-equipped turbine at azimuth angles of 90° and 135° further reinforces the improvements in torque and efficiency of this configuration. It is also notable that a positive pressure difference of about 100 Pa is observed on the suction side of the rotor blade set with a double deflector at an azimuth angle of 135° , leading to a more effective rotor torque. When the rotor is rotated and located at the downwind area where the blade sets are placed at azimuth angles of 225° and 285° , it is observed that the pressure distribution on the suction and pressure sides of the blades in both configurations is nearly identical. This indicates that the pressure distribution in this position does not significantly contribute to the rotor's performance improvement. The negative pressure of -150 Pa on the suction side of the auxiliary blade equipped with a double deflector at an azimuth angle of 285° suggests that the high-velocity area and the formation of a negative vorticity lead to a swirling flow and flow separation due to the sharp angle of attack, which have occurred in this particular position. Therefore, the validity of a velocity and vorticity field is confirmed based on the pressure distribution in this section.

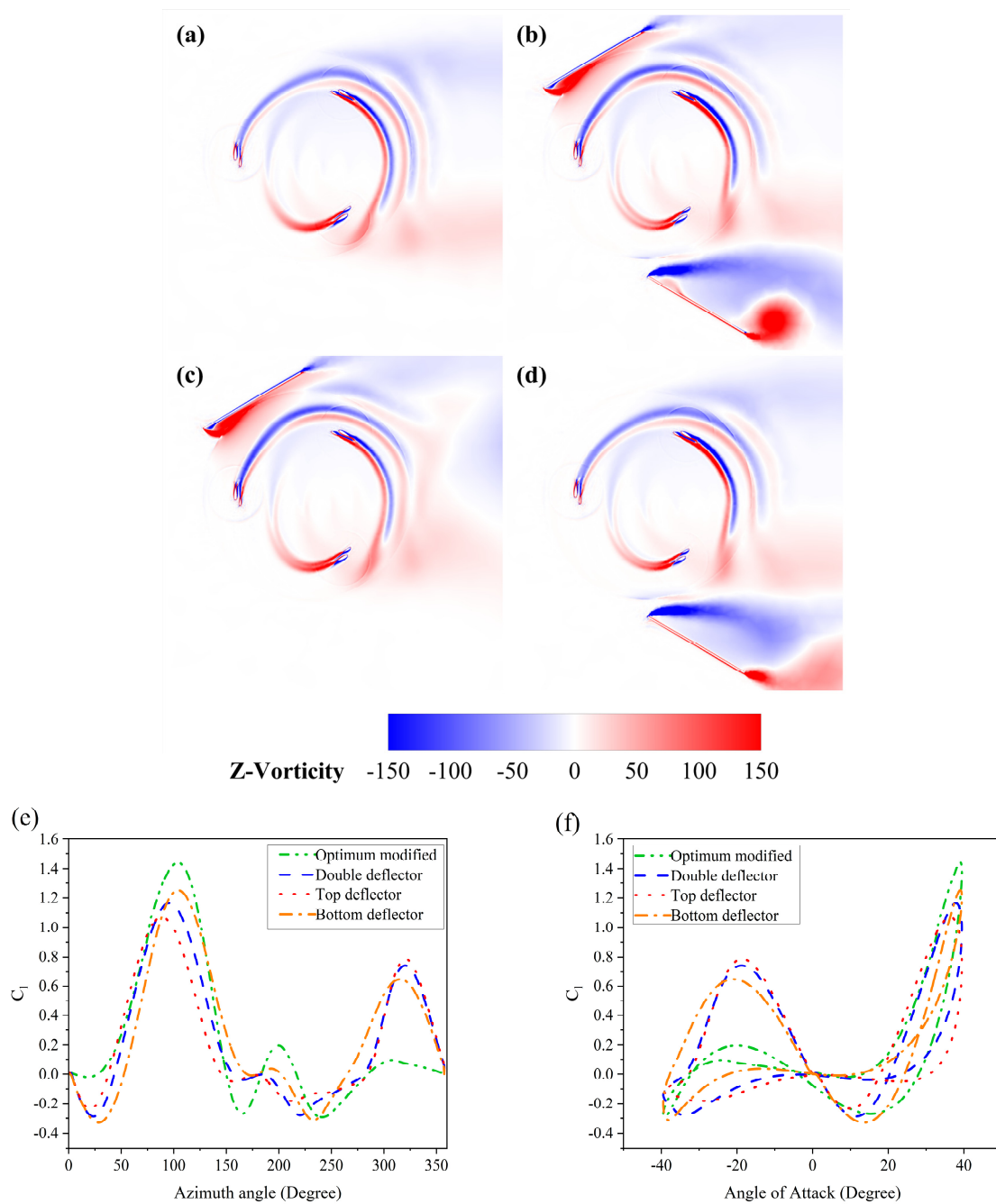


Figure 19. Z-vorticity contour plot for (a) optimum modified rotor, (b) double deflector, (c) top deflector, (d) bottom deflector at $TSR = 2.6$ and $\theta = 90^\circ$, (e) lift coefficient variation over a complete rotation, and (f) lift coefficient variation as a function of AoA.

In Figure 21, the optimal rotor torque with and without a double deflector in a full rotation are compared. At a 0° azimuth angle, the torque did not exhibit significant differences. The findings indicate that the deflector does not enhance the rotor's performance within the low- TSR range and is ineffective in facilitating self-starting. This observation corroborates the results presented in the performance map illustrated in Figure 17. During the rotor rotation, it was observed that the rotor's torque with the double deflector surpassed the optimal torque of the rotor without the deflector within the azimuth angles ranging from 25° to 140° . This observation also substantiates the presence of pressure differences on the blade set suction and pressure sides at azimuth angles of 45° , 90° , and 135° . Furthermore, at azimuth angles from 140° to 360° , the torque of both rotors is nearly equal to each other,

confirming the consistent pressure gradient distribution, as shown in Figure 20 at azimuth angles of 225° and 285°. It is noticeable that the positive impact of the deflector installation was limited to azimuth angles below 140°.

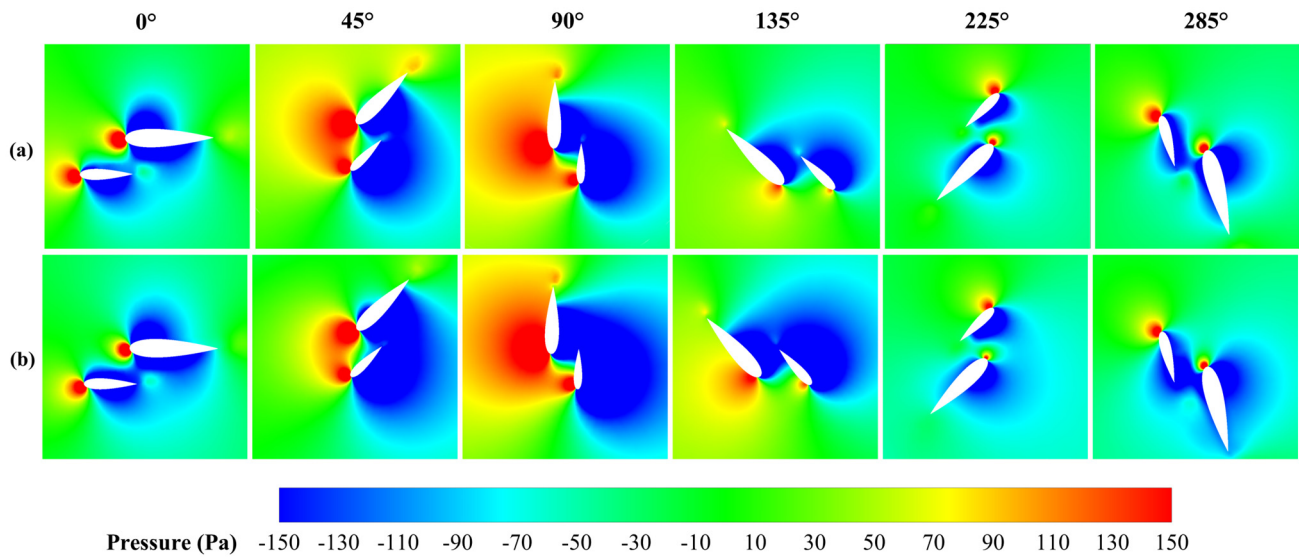


Figure 20. Pressure distribution for one blade set: (a) modified Darrieus VAWT and (b) modified Darrieus VAWT with double deflector for TSR = 1.4.

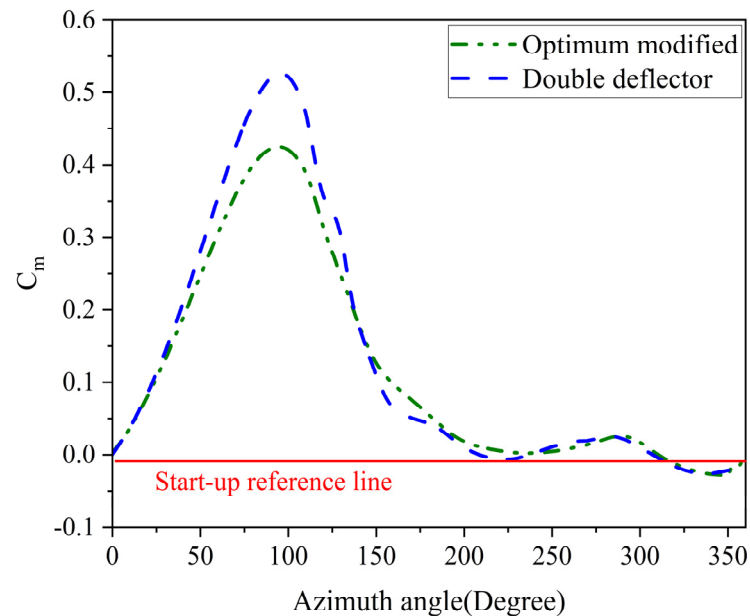


Figure 21. Variation of C_m over a complete rotation considering optimum modified rotor with and without double deflector at TSR = 2.6.

5. Conclusions

In this investigation, a 2D model of the Darrieus VAWT was selected as a control case and subjected to CFD analysis using URANS flow equations and the $k - \omega$ SST turbulence model after grid generation for discretization. Following verification through three validation studies encompassing mesh number independence, time-step independence, and comparison with prior numerical and experimental findings, the validity of the chosen model was substantiated. Auxiliary blades with different positions were incorporated to enhance the Darrieus rotor's self-starting capability. Furthermore, to optimize the rotor's efficiency and address potential inefficiencies at high rotation speeds, the impact of installing

deflectors with different arrangements in front of the rotor, equipped with an auxiliary blade, was assessed. Installing the auxiliary blade expanded the rotor's operating range in the low-TSR range and reduced the starting TSR from 1.4 to 0.7, showing self-starting capability improvement. The accuracy of this modification was confirmed by analyzing the pressure distribution around the blades. Three conceptual design parameters were considered to optimize the installation of the auxiliary blade: pitch angle, horizontal distance, and vertical distance from the main blade. The study revealed that a pitch angle of 0° resulted in the most significant improvement in rotor efficiency, increasing the C_p value by 59% at $TSR = 1.4$. Investigations into the horizontal and vertical distances between the auxiliary blade and the main blade have demonstrated that setting $X = 44.2$ mm or $X/C = 0.52$ and $Y = 34.9$ mm or $Y/C = 0.41$ enhances the self-starting capability and improves C_p in the TSR range. Furthermore, the consideration of these values minimally impacts the rotor's performance in the high-TSR range. The presence of the auxiliary blade in the low-TSR range only has notably enhanced the rotor's self-starting capability by improving efficiency and static torque. However, the presence of the auxiliary blade at a high-TSR range, when the blade sets are in the downwind position and the angle of attack is sharp, has led to flow separation and swirl flow, thus impacting the rotor's performance. The installation of a deflector was examined as a potential solution to mitigate this issue. According to the performance map analysis, among the three configurations of double, top, and bottom deflectors, the installation of the double deflector effectively addressed the potential issue with the rotor equipped with an auxiliary blade, resulting in a notable 73% improvement in C_p . Conversely, the installation of the deflector did not contribute to enhancing the self-starting capability. Installing the top deflector at $TSR = 1.4$ led to a 71% decrease in C_p compared to the rotor without the deflector. It is essential to clarify that the Betz limit has been consistently adhered to throughout all stages of the simulation, including the addition of an auxiliary blade and the incorporation of a deflector in various configurations. This limit, which serves as a benchmark for the efficiency of wind turbines, is defined as approximately 0.5 for HAWTs and around 0.7 for VAWTs [56]. The performance map indicates that the maximum value of the C_p has not surpassed this established threshold.

Finally, a comparative analysis shows that the findings of the current CFD study align with those of prior research. Mohamed et al. [14] indicated that at $TSR < 1.5$, the challenge of self-starting becomes significantly more pronounced. In this context, the installation of auxiliary blades extended this value to $TSR = 0.7$. Furthermore, they asserted that the self-starting capability of the rotor exhibited improvement between azimuth angles of 90° and 180° . Our recent study observed that the most notable enhancement occurred due to the implementation of auxiliary blades within a semi-similar range, specifically between 60° and 170° . Also, Celik et al. [13] successfully enhanced the self-starting capability by incorporating additional blades; however, they observed decreased peak C_p in configurations featuring more blades. This observation supports the phenomenon of blade-to-blade interaction, which was noted in the recent study between the main blade and auxiliary blades. Despite the improvements in self-starting capability, C_p and the C_l diminished at the high-TSR range.

6. Future Studies

The present study aims to provide a comprehensive examination of the combined effects of auxiliary blades and deflectors across various configurations to enhance self-starting capabilities and overall efficiency within both low and high-TSR ranges. However, several recommendations for future research remain. It is advisable to conduct wind tunnel tests on various auxiliary blade configurations, utilizing different pitch angles and both horizontal and vertical distances. The findings of these tests should be evaluated in a detailed analysis prior to commercialization. For enhanced numerical accuracy, it is advisable to develop 3D geometry and employ the Large Eddy Simulation (LES) methodology for a more precise examination of flow physics. Furthermore, it is recommended to integrate different external objects, such as curtains, control rods, and semi- or omnidirectional guide vanes. To gain a

thorough understanding of the efficiency associated with this configuration, a comparative analysis of the Darrieus VAWT design, in conjunction with an auxiliary blade or incorporating a dual rotor system, or a Savonius–Darrieus hybrid turbine, may be undertaken. This analysis will enable a discussion concerning each design’s relative advantages based on the flow physics information. It is important to acknowledge that, based on the rotor diameter of approximately 1 (m), this VAWT can be considered larger than a typical laboratory prototype and possesses the potential to function as a commercial turbine in real-world applications. Consequently, the results obtained are applicable to practical scenarios. The integration of such a VAWT, in conjunction with deflectors and auxiliary blades, could lead to significant advancements in engineering design by improving the self-starting capability and aerodynamic performance when installed on the roofs of high-rise buildings, along highways, and on ocean-going vessels.

Author Contributions: Conceptualization, F.G.; methodology, F.G.; software, E.E.; validation, F.G. and S.R.M.; formal analysis, F.G. and H.W.; investigation, F.G. and E.E.; resources, F.G.; data curation, F.G., S.R.M. and E.E.; writing—original draft preparation, F.G.; writing—review and editing, F.G., E.E. and H.W.; visualization, E.E.; supervision, F.G. and H.W.; project administration, F.G. and H.W.; funding acquisition, F.G. and H.W. All authors have read and agreed to the published version of the manuscript.

Funding: This research received no external funding.

Data Availability Statement: The data that support the findings of this study are available in this paper.

Conflicts of Interest: The authors declare no conflict of interest.

Nomenclature

Symbols		Subscript	
V_∞	Inlet flow velocity (m/s)	t	Turbulence
A	Swept Area (m ²)	Abbreviations	
T	Torque (N·m)	VAWT	Vertical axis wind turbine
P	Output power (W)	HAWT	Horizontal axis wind turbine
R	Rotor radius (m)	CFD	Computational fluid dynamic
H	Rotor height (m)	C_{FL}	Courant number
C_p	Power coefficient	URANS	Unsteady Reynolds averaged Naiver–Stokes
C_m	Torque coefficient	TSR	Tip speed ratio
C_l	Lift coefficient		
n	Number of blades		
c	Blade chord length		
Greek			
θ	Azimuth angle (Degree)		
μ	Viscosity (Pa.s)		
Ω	Angular velocity (rad/s)		
ρ	Density (kg/m ³)		
σ	Rotor solidity		

References

1. Kumar, Y.; Roga, S.; Wanmali, N.K. Experimental analysis of hybrid VAWT and the effect of semi-cylindrical attachment to the trailing edge. *Energy Sustain. Dev.* **2023**, *74*, 115–126. [CrossRef]
2. IEA. World Energy Outlook 2022—Analysis. Available online: <https://www.iea.org/reports/world-energy-outlook-2022> (accessed on 11 June 2024).
3. Zidane, I.F.; Ali, H.M.; Swadener, G.; Eldrainy, Y.A.; Shehata, A.I. Effect of upstream deflector utilization on H-Darrieus wind turbine performance: An optimization study. *Alex. Eng. J.* **2023**, *63*, 175–189. [CrossRef]
4. Fazylova, A.; Tultayev, B.; Iliiev, T.; Stoyanov, I.; Kabasheva, M.; Kosunalp, S. Experimental Study of an Industrial Data Transmission Network in the Automatic Control System of a Wind Turbine. *Machines* **2024**, *12*, 746. [CrossRef]

5. Tahani, M.; Rabbani, A.; Kasaeian, A.; Mehrpooya, M.; Mirhosseini, M. Design and numerical investigation of Savonius wind turbine with discharge flow directing capability. *Energy* **2017**, *130*, 327–338. [[CrossRef](#)]
6. Pope, K.; Dincer, I.; Naterer, G.F. Energy and exergy efficiency comparison of horizontal and vertical axis wind turbines. *Renew. Energy* **2010**, *35*, 2102–2113. [[CrossRef](#)]
7. Efendi, M.Y.; Amir, N.; Prasetyo, T.; Ramadhan, M.Y.A.; Gozan, M.; Darmawan, M.A.; Alhamid, M.I. Experimental and simulation investigation of a Savonius vertical axis wind turbine for residential applications: A case study in Indonesia. *Int. J. Ambient Energy* **2024**, *45*, 2331231. [[CrossRef](#)]
8. Pouransari, Z.; Behzad, M. Numerical investigation of the aerodynamic performance of a hybrid Darrieus-Savonius wind turbine. *Wind Eng.* **2024**, *48*, 3–14. [[CrossRef](#)]
9. Hosseini, A.; Goudarzi, N. Design and CFD study of a hybrid vertical-axis wind turbine by employing a combined Bach-type and H-Darrieus rotor systems. *Energy Convers. Manag.* **2019**, *189*, 49–59. [[CrossRef](#)]
10. Arpino, F.; Scungio, M.; Cortellessa, G. Numerical performance assessment of an innovative Darrieus-style vertical axis wind turbine with auxiliary straight blades. *Energy Convers. Manag.* **2018**, *171*, 769–777. [[CrossRef](#)]
11. Jacob, J.; Chatterjee, D. Design methodology of hybrid turbine towards better extraction of wind energy. *Renew. Energy* **2019**, *131*, 625–643. [[CrossRef](#)]
12. Farajyar, S.; Ghafoorian, F.; Mehrpooya, M.; Asadbeigi, M. CFD Investigation and Optimization on the Aerodynamic Performance of a Savonius Vertical Axis Wind Turbine and Its Installation in a Hybrid Power Supply System: A Case Study in Iran. *Sustainability* **2023**, *15*, 5318. [[CrossRef](#)]
13. Celik, Y.; Ma, L.; Ingham, D.; Pourkashanian, M. Aerodynamic investigation of the start-up process of H-type vertical axis wind turbines using CFD. *J. Wind Eng. Ind. Aerodyn.* **2020**, *204*, 104252. [[CrossRef](#)]
14. Mohamed, O.S.; Elbaz, A.M.R.; Bianchini, A. A better insight on physics involved in the self-starting of a straight-blade Darrieus wind turbine by means of two-dimensional Computational Fluid Dynamics. *J. Wind Eng. Ind. Aerodyn.* **2021**, *218*, 104793. [[CrossRef](#)]
15. Abbasi, S.; Daraee, M.A. Improving vertical-axis wind turbine performance through innovative combination of deflector and plasma actuator. *Phys. Fluids* **2024**, *36*, 045134. [[CrossRef](#)]
16. Redchyt, D.; Portal-Porras, K.; Tarasov, S.; Moiseienko, S.; Tuchyna, U.; Starun, N.; Fernandez-Gamiz, U. Aerodynamic Performance of Vertical-Axis Wind Turbines. *J. Mar. Sci. Eng.* **2023**, *11*, 1367. [[CrossRef](#)]
17. Jiang, T.; Zhao, Y.; Wang, S.; Zhang, L.; Li, G. Aerodynamic characterization of a H-Darrieus wind turbine with a Drag-Disturbed Flow device installation. *Energy* **2024**, *292*, 130522. [[CrossRef](#)]
18. Ghafoorian, F.; Mirmotahari, S.R.; Mehrpooya, M.; Akhlaghi, M. Aerodynamic performance and efficiency enhancement of a Savonius vertical axis wind turbine with Semi-Directional Curved Guide Vane, using CFD and optimization method. *J. Braz. Soc. Mech. Sci. Eng.* **2024**, *46*, 443. [[CrossRef](#)]
19. Ghafoorian, F.; Mirmotahari, S.R.; Wan, H. Numerical study on aerodynamic performance improvement and efficiency enhancement of the savonius vertical axis wind turbine with semi-directional airfoil guide vane. *Ocean Eng.* **2024**, *307*, 118186. [[CrossRef](#)]
20. Saikot, M.M.H.; Rahman, M.; Hosen, M.A.; Ajwad, W.; Jamil, M.F.; Islam, M.Q. Savonius Wind Turbine Performance Comparison with One and Two Porous Deflectors: A CFD Study. *Flow Turbul. Combust.* **2023**, *111*, 1227–1251. [[CrossRef](#)]
21. Layeghmand, K.; Tabari, N.G.; Zarkesh, M. Improving efficiency of Savonius wind turbine by means of an airfoil-shaped deflector. *J. Braz. Soc. Mech. Sci. Eng.* **2020**, *42*, 528. [[CrossRef](#)]
22. Chitura, A.G.; Mukumba, P.; Lethole, N. Enhancing the Performance of Savonius Wind Turbines: A Review of Advances Using Multiple Parameters. *Energies* **2024**, *17*, 3708. [[CrossRef](#)]
23. Schaffarczyk, A.P.; Lobo, B.A.; Balaesque, N.; Kremer, V.; Suhr, J.; Wang, Z. Development and Measurement of a Very Thick Aerodynamic Profile for Wind Turbine Blades. *Wind* **2024**, *4*, 190–207. [[CrossRef](#)]
24. Mazarbhuiya, H.M.S.M.; Sengupta, A.R.; Biswas, A.; Sharma, K.K. Wind tunnel investigation of blade pitch effect for performance improvement of an asymmetric bladed H-Darrieus VAWT under low wind speed condition. *Int. J. Ambient Energy* **2024**, *45*, 2277300. [[CrossRef](#)]
25. Naik, K.; Sahoo, N. Aerodynamic performance and starting torque enhancement of small-scale Darrieus type straight-bladed vertical axis wind turbines with J-shaped airfoil. *J. Renew. Sustain. Energy* **2024**, *16*, 033304. [[CrossRef](#)]
26. Mălăeș, I.; Strătilă, S. High-Precision Numerical Investigation of a VAWT Starting Process. *Processes* **2024**, *12*, 2263. [[CrossRef](#)]
27. Korukçu, M.Ö. Impact of Blade Modifications on the Performance of a Darrieus Wind Turbine. *Processes* **2024**, *12*, 732. [[CrossRef](#)]
28. Javaid, M.T.; Sajjad, U.; ul Hassan, S.S.; Nasir, S.; Shahid, M.U.; Ali, A.; Salamat, S. Power enhancement of vertical axis wind turbine using optimum trapped vortex cavity. *Energy* **2023**, *278*, 127808. [[CrossRef](#)]
29. Tayebi, A.; Torabi, F. Flow control techniques to improve the aerodynamic performance of Darrieus vertical axis wind turbines: A critical review. *J. Wind Eng. Ind. Aerodyn.* **2024**, *252*, 105820. [[CrossRef](#)]
30. Ibrahim, A.A.; Elbaz, A.M.R.; Melani, P.F.; Mohamed, O.S.; Bianchini, A. Power augmentation of Darrieus wind turbine blades using trapped vortex cavity. *J. Wind Eng. Ind. Aerodyn.* **2022**, *223*, 104949. [[CrossRef](#)]
31. Iddou, H.; Bouda, N.N.; Benaissa, A.; Zereg, K. Numerical Analysis of the Kline and Fogleman Airfoil's Effect on the Operation of Straight Darrieus Wind Turbine. *J. Appl. Fluid Mech.* **2024**, *17*, 1568–1592.

32. Tahani, M.; Razavi, M.; Mirhosseini, M.; Astarai, F.R. Unsteady aerodynamic performance of Dual-Row H-Darrieus vertical axis wind turbine. *Energy Equip. Syst.* **2020**, *8*, 55–80.
33. Khalid, M.S.U.; Wood, D.; Hemmati, A. Self-Starting Characteristics and Flow-Induced Rotation of Single- and Dual-Stage Vertical-Axis Wind Turbines. *Energies* **2022**, *15*, 9365. [[CrossRef](#)]
34. Khalid, M.S.U.; Mendoza, P.S.P.; Wood, D.; Hemmati, A. On the aerodynamics of dual-stage co-axial vertical-axis wind turbines. *Wind Eng.* **2024**, *48*, 408–424. [[CrossRef](#)]
35. Shen, Z.; Gong, S.; Xie, G.; Lu, H.; Guo, W. Investigation of the effect of critical structural parameters on the aerodynamic performance of the double darrieus vertical axis wind turbine. *Energy* **2024**, *290*, 130156. [[CrossRef](#)]
36. Asadbeigi, M.; Ghafoorian, F.; Mehrpooya, M.; Chegini, S.; Jarraghan, A. A 3D Study of the Darrieus Wind Turbine with Auxiliary Blades and Economic Analysis Based on an Optimal Design from a Parametric Investigation. *Sustainability* **2023**, *15*, 4684. [[CrossRef](#)]
37. Reddy, K.U.; Deb, B.; Roy, B. Experimental Study on Influence of Aspect Ratio and Auxiliary Blade Profile on the Performance of H-Type Darrieus Wind Rotor. *Arab. J. Sci. Eng.* **2024**, *49*, 1913–1929. [[CrossRef](#)]
38. Castelli, M.R.; Englaro, A.; Benini, E. The Darrieus wind turbine: Proposal for a new performance prediction model based on CFD. *Energy* **2011**, *36*, 4919–4934. [[CrossRef](#)]
39. Ghafoorian, F.; Mirmotahari, S.R.; Eydizadeh, M.; Mehrpooya, M. A systematic investigation on the hybrid Darrieus-Savonius vertical axis wind turbine aerodynamic performance and self-starting capability improvement by installing a curtain. *Next Energy* **2025**, *6*, 100203. [[CrossRef](#)]
40. Sheidani, A.; Salavatidezfouli, S.; Stabile, G.; Rozza, G. Assessment of URANS and LES methods in predicting wake shed behind a vertical axis wind turbine. *J. Wind Eng. Ind. Aerodyn.* **2023**, *232*, 105285. [[CrossRef](#)]
41. Menter, F.R. Review of the shear-stress transport turbulence model experience from an industrial perspective. *Int. J. Comput. Fluid Dyn.* **2009**, *23*, 305–316. [[CrossRef](#)]
42. Didane, D.H.; Rosly, N.; Zulkafli, M.F.; Shamsudin, S.S. Numerical investigation of a novel contra-rotating vertical axis wind turbine. *Sustain. Energy Technol. Assess.* **2019**, *31*, 43–53. [[CrossRef](#)]
43. Borzuei, D.; Moosavian, S.F.; Farajollahi, M. On the Performance Enhancement of the Three-Blade Savonius Wind Turbine Implementing Opening Valve. *J. Energy Resour. Technol.* **2020**, *143*, 1–30. [[CrossRef](#)]
44. Bianchini, A.; Balduzzi, F.; Bachant, P.; Ferrara, G.; Ferrari, L. Effectiveness of two-dimensional CFD simulations for Darrieus VAWTs: A combined numerical and experimental assessment. *Energy Convers. Manag.* **2017**, *136*, 318–328. [[CrossRef](#)]
45. Rezaeiha, A.; Kalkman, I.; Blocken, B. Effect of pitch angle on power performance and aerodynamics of a vertical axis wind turbine. *Appl. Energy* **2017**, *197*, 132–150. [[CrossRef](#)]
46. Lositaño, I.C.M.; Danao, L.A.M. Steady wind performance of a 5 kW three-bladed H-rotor Darrieus Vertical Axis Wind Turbine (VAWT) with cambered tubercle leading edge (TLE) blades. *Energy* **2019**, *175*, 278–291. [[CrossRef](#)]
47. Marsh, P.; Ranmuthugala, D.; Penesis, I.; Thomas, G. The influence of turbulence model and two and three-dimensional domain selection on the simulated performance characteristics of vertical axis tidal turbines. *Renew. Energy* **2017**, *105*, 106–116. [[CrossRef](#)]
48. Ahmad, T.; Plee, S.L.; Myers, J.P. *FLUENT User's Guide*; ANSYS, Inc.: Canonsburg, PA, USA, 2010
49. Trentin, P.F.S.; Martinez, P.H.B.D.B.; Santos, G.B.D.; Gasparin, E.E.; Salviano, L.O. Screening analysis and unconstrained optimization of a small-scale vertical axis wind turbine. *Energy* **2022**, *240*, 122782. [[CrossRef](#)]
50. Roache, P.J. Quantification of Uncertainty in Computational Fluid Dynamics. *Annu. Rev. Fluid Mech.* **1997**, *29*, 123–160. [[CrossRef](#)]
51. Balduzzi, F.; Bianchini, A.; Ferrara, G.; Ferrari, L. Dimensionless numbers for the assessment of mesh and timestep requirements in CFD simulations of Darrieus wind turbines. *Energy* **2016**, *97*, 246–261. [[CrossRef](#)]
52. Trivellato, F.; Castelli, M.R. On the Courant–Friedrichs–Lewy criterion of rotating grids in 2D vertical-axis wind turbine analysis. *Renew. Energy* **2014**, *62*, 53–62. [[CrossRef](#)]
53. Chegini, S.; Asadbeigi, M.; Ghafoorian, F.; Mehrpooya, M. An investigation into the self-starting of darrieus-savonius hybrid wind turbine and performance enhancement through innovative deflectors: A CFD approach. *Ocean Eng.* **2023**, *287*, 115910. [[CrossRef](#)]
54. Tescione, G.; Ragni, D.; He, C.; Ferreira, C.J.S.; Van Bussel, G.J.W. Near wake flow analysis of a vertical axis wind turbine by stereoscopic particle image velocimetry. *Renew. Energy* **2014**, *70*, 47–61. [[CrossRef](#)]
55. Qamar, S.B.; Janajreh, I. A comprehensive analysis of solidity for cambered darrieus VAWTs. *Int. J. Hydrogen Energy* **2017**, *42*, 19420–19431. [[CrossRef](#)]
56. Dixon, S.L.; Hall, C.A. *Fluid Mechanics and Thermodynamics of Turbomachinery*, 7th ed.; Butterworth-Heinemann: Amsterdam, The Netherlands; Boston, MA, USA, 2014.

Disclaimer/Publisher's Note: The statements, opinions and data contained in all publications are solely those of the individual author(s) and contributor(s) and not of MDPI and/or the editor(s). MDPI and/or the editor(s) disclaim responsibility for any injury to people or property resulting from any ideas, methods, instructions or products referred to in the content.